Plasma Sources Science and Technology

PAPER

Numerical investigation of discharge evolution and breakdown characteristics of ArF excimer lasers

To cite this article: Xiaochi Ma *et al* 2024 *Plasma Sources Sci. Technol.* **33** 075012

IOP Publishing Plasma Sources Science and Technology
Plasma Sources Sci. Technol. **33** (2024) 075012 (22pp) https://doi.org/10.1088/1361-6595/ad5df6

Numerical investigation of discharge evolution and breakdown characteristics of ArF excimer lasers

Xiaochi Ma[1], Luying Bai[1], Yifei Zhu[1,*], Xinxian Jiang[2,*] and Yun Wu[1]

[1] National Key Lab of Aerospace Power System and Plasma Technology, Xi'an Jiaotong University, Xi'an 710049, People's Republic of China
[2] Beijing RSLaser Opto-Electronics Technology Co., Ltd, Beijing 100176, People's Republic of China

E-mail: yifei.zhu.plasma@gmail.com and jxx052310382@126.com

Received 19 January 2024, revised 31 May 2024
Accepted for publication 2 July 2024
Published 22 July 2024

Abstract

The corona bar induced pre–ionization is a crucial preliminary process in the operation of ArF excimer lasers, directly impacting the uniformity and stability of output laser. The ultraviolet corona pre–ionization, as the mainstream method, is tightly coupled with the main discharge process, which complicates analysis. Here, we establish a numerical model of a single pulse discharge incorporating an external circuit to analyze the pre–ionization process and its influence on the breakdown characteristics. (1) By adopting detailed input parameters of photoionization model, we observe uniform and dispersed plasma propagation from the corona bar to the main gap. (2) An artificial boundary condition is proposed to investigate the phenomenological effect of high–energy electrons emission, emphasizing the influence of surface discharge along the cathode. (3) The propagation and breakdown characteristics of the two pre–ionization setup methods, photoionization and background electron density, are compared numerically. This study enhances the understanding of the pre–ionization process in ArF excimer lasers and provides theoretical insights for their optimization and design.

Keywords: ArF excimer lasers, plasma, numerical model, pre–ionization

1. Introduction

ArF excimer lasers, operating at a wavelength of 193 nm, are extensively used across various scientific and industrial domains, including DUV photolithography [1–3], micro/nano manufacturing [4–6], refractive surgery [7], laser fusion ignition [8, 9], etc due to their low wavelength and high energy characteristics. The plasma driven by high–voltage pulses to take place the electron impact excitation and ionization in the discharge chamber of ArF excimer lasers, is essential laser generation process.

Unstable discharge in excimer lasers can lead to localized hotspots [10], filaments, and arc transitions [11], all of which diminish the laser strength. To maintain a consistent, stable, and repeatable excimer laser over extended periods, it is crucial to sustain the discharge in a continuous glow state as much as possible. This necessitates an adequate background electron density to ensure a uniform electric field before initiating the main discharge, often referred to as pre–ionization. Therefore, the pre–ionization subsystem in excimer lasers is indispensable [3]. Various methods have been employed to facilitate pre–ionization in excimer lasers, such as X–ray radiation [12, 13], laser beam [14–16], electron beam [17–20], and UV/VUV radiation [21, 22], and researchers have investigated the intensity, timing, and mechanism of pre–ionization.

In previous research, due to the decoupling between pre–ionization and the main discharge, it is convenient to control the intensity and time delay of pre–ionization to achieve the strongest laser. Based on this notion, there are related experimental studies: Delmdahl *et al* mentioned in their review [21] that the UV light produced by spark discharge pre–ionization

* Authors to whom any correspondence should be addressed.

can generate a uniform electron density of 10^{14} m^{-3} at 10 ns before the main discharge starts. D Mathew *et al* investigated the F_2 excimer laser with X–ray pre–ionization [12], and they believed that a density of 10^{13} m^{-3}/bar ensures discharge uniformity, with the optimal triggering time difference in their device being 20 ns. L Feenstra *et al* investigated the pre–ionization of ArF and KrF [23], indicating that imposing pre–ionization at 60 ns before breakdown proves most effective. It can be seen that diverse outcomes are affected by the pre–ionization methods, gas compositions, and structural considerations, which significantly influence the optimal parameters for pre–ionization in laser systems.

Moreover, there are focused explorations into the underlying physical mechanisms governing pre–ionization in excimer lasers. On the one hand, the generation of pre–ionization has gained attention: D Levko explored the roles of runaway electrons, X–ray, and photoionization in pre–ionization [24, 25] and evaluated their relative importance. Azarov *et al* investigated the photoelectric effect in X–ray pre–ionization [26]. Depending on the different pressure, gas ratio, and electrode gap, the pre–ionization can be based on different mechanisms, with fast electrons emitted from the cathode sometimes playing the dominant role. Additionally, pre–ionization can change the propagation of plasma, including the propagating direction [27] and suppressing plasma branching [15]. On the other hand, currently, with the increasing demands of users for the power, frequency, and compactness of excimer laser products, the corona discharge pre–ionization coupled with the main discharge has become one of the mainstream methods. Analyzing the plasma process in this context requires a comprehensive consideration of both pre–ionization and the main discharge, which poses difficulties for experimental diagnosis. Therefore, numerical simulations are gradually being developed in the field of excimer lasers.

The discharge numerical simulations of excimer lasers mainly rely on kinetics calculation [23, 28–30] (0D), and some focus on the plasma in the main gap [31–33] (1D, 2D). Research encompassing both pre–ionization and the main discharge coupling processes remains exceptionally scarce. Only Xiong and Mark J Kushner's work has ventured into investigating the complete pre–ionization [34] and discharge process [35] of ArF excimer lasers (2D) first of all. They discussed the pre–avalanche photo–generated electron density is about 10^8 cm^{-3}, and the critical role of sheath–accelerated secondary electrons in ArF excimer Lasers.

In this paper, the discharge evolution in one single pulse of ArF excimer lasers is studied. (1) Different from previous work, we adopt a detailed input parameters in the photoionization model, and reevaluate the critical role of photo–generated electrons in propagation and breakdown. Based on the external circuit model, the computational electrical parameters are compared with experimental results to validate the numerical model. (2) To investigate the disparities between simulation and experiment, an artificial boundary condition (BC) is applied to replace the electronic Monte Carlo Simulation (eMCS) in plasma–fluid framework, simulating the phenomenology of high–energy electrons emission. (3) A comparison of the differences between the background ionization and the photoionization is investigated. The numerical model is described in section 2, followed by a discussion of the simulation results in section 3. Finally, a summary is provided in section 4.

2. Numerical model description

2.1. Geometry and mesh

The partial 2D section diagram of ArF excimer lasers is shown in figure 1(a), which includes the cathode (copper, colored in red), anode (copper, colored in blue), dielectric (alumina ceramic, colored in green, the relative permittivity $\varepsilon/\varepsilon_0 = 8$, ε_0 is the vacuum permittivity), and the plasma region (colored in white). Figure 1(a) only contains the components that are relevant to the computational results, while neglecting those that are not important. It is worth mentioning that the corona bar is included in the computational domain, as it plays a significant role in providing photo–generated electrons for the main gap.

The numerical model employs the structured adaptive mesh refinement in a 2D Cartesian coordinate system. The mesh is initialized based on the geometry shape shown in figure 1(b). The criteria for adaptive mesh refinement is based on the electron density:

$$h = h_{\max} \times \frac{1}{2^n} \leqslant max\left(\frac{\log_{10}(n_e)}{18} h_{\min} - \frac{18 - \log_{10}(n_e)}{18} h_{\max}, h_{min}\right) \tag{1}$$

where h is the mesh size, n_e is the electron density, $h_{\min}$, $h_{\max}$ are the minimal and maximum mesh size, and n is the number of refinement times, respectively. To distinguish the space charge, we estimated the Debye length λ_D:

$$\lambda_D \equiv \sqrt{\frac{\varepsilon_0 k_b T_e}{n_e e^2}} \approx 3.7 \times 10^{-6}\ \mathrm{m} \tag{2}$$

where k_b is the Boltzmann constant, $T_e \approx 5$ eV is the estimated electron temperature, $n_e \approx 2 \times 10^{20}$ m^{-3} is the estimated electron density, and e is the elementary charge. We set $h_{\min} = 5 \times 10^{-6}$ m, $h_{\max} = 1 \times 10^{-3}$ m to keep the refined mesh size and the Debye length in the same order of magnitude:

$$h_{\text{refined}} = 1 \times 10^{-3} \times \frac{1}{2^8} \approx 3.9 \times 10^{-6}\ \mathrm{m} < 5.0 \times 10^{-6}\ \mathrm{m}. \tag{3}$$

2.2. Governing equations and BCs

The 2D plasma–fluid code *PASSKEy* (PArallel Streamer Solver with KinEtics) is used in this study for modeling the nanosecond discharge in ArF excimer lasers. Compared to the local field approximation, it has been demonstrated in previous studies [36, 37] that the local mean energy approximation (LMEA) provides greater accuracy in electron density and is more suitable for atmosphere pressure simulations. Hence, the LMEA is adopted in our model, and the code validation has

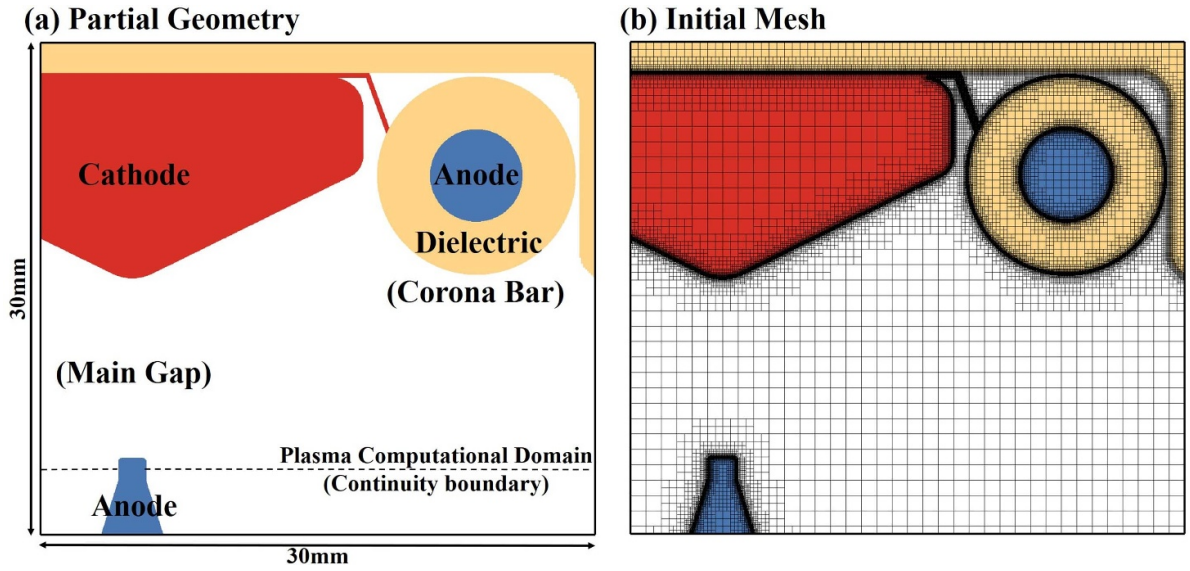

Figure 1. (a) The partial 2D section diagram of ArF excimer lasers, and (b) the initial meshes with geometric refinement.

been carried out in published work [38, 39]. The equations employed in the model are presented below.

The species drift–diffusion equation is:

$$\frac{\partial n_i}{\partial t} + \nabla \cdot \mathbf{\Gamma}_i = S_i + S_{\text{ph}},\ i = 1,2,\ldots,N_{\text{total}} \tag{4}$$

where n_i is the number density of species i, t is time, S_i is the reaction source term of species i, S_{ph} is the photoionization source term, $\mathbf{\Gamma}_i$ is the plasma component flux caused by drift and diffusion, and its expression is:

$$\mathbf{\Gamma}_i = (q_i/|q_i|)\,\mu_i n_i \boldsymbol{E} - D_i \nabla n_i, i = 1,2,\ldots,N_{\text{charge}} \tag{5}$$

where q_i is the charge number of species i, D_i is the diffusion coefficient and μ_i is the mobility of species i, respectively. $\boldsymbol{E}$ is the electric field. The diffusion coefficient and mobility of electron are calculated using BOLSIG+[40]. The mobility of ions is determined using MOBION [41], while the diffusion coefficients are determined using the Einstein relationship:

$$D = \mu\,(k_b T/e),\quad k_b = 1.38\times10^{-23} J/K, e = 1.602\times10^{-19} C. \tag{6}$$

The electron energy conservation equation is:

$$\frac{\partial n_e \epsilon_m}{\partial t} + \nabla \cdot \mathbf{\Gamma}_\epsilon = -|q_e| \cdot \mathbf{\Gamma}_e \cdot \boldsymbol{E} - P(\epsilon_m) \tag{7}$$

where n_e is the electron density, ϵ_m is the mean electron energy, $\mathbf{\Gamma}_\epsilon$ and $\mathbf{\Gamma}_e$ are the fluxes of electron energy and electron, respectively, and $P(\epsilon_m)$ is the power by collisions. The expression for $\mathbf{\Gamma}_\epsilon$ is:

$$\mathbf{\Gamma}_\epsilon = -\mu_\epsilon n_e \epsilon_m \boldsymbol{E} - D_\epsilon \nabla (n_e \epsilon_m) \tag{8}$$

where μ_ϵ is the electron energy mobility, and D_ϵ is the electron energy diffusion coefficient.

The electric field is determined by solving the Poisson equation coupled with space charge:

$$\nabla (\varepsilon_0 \varepsilon_r (-\nabla \Phi)) = -\rho - \rho_c \tag{9}$$

$$\boldsymbol{E} = -\nabla \Phi \tag{10}$$

$$\rho = \sum_{i=1}^{N_{ch}} n_i q_i \tag{11}$$

$$\frac{\partial \rho_c}{\partial t} = \sum_{i=1}^{N_{ch}} q_i (-\nabla \cdot \mathbf{\Gamma}_i) \tag{12}$$

where ε_0 is the vacuum permittivity, ε_r is the relative permittivity, Φ is the potential, $\boldsymbol{E}$ is the electric field, ρ is the space charge, and ρ_c is the surface charge determined by the flux of ions $\mathbf{\Gamma}_{\text{ion}}$ at the interfaces between the plasma and the dielectric. Due to the curvature of the electrode and the electric field enhancement are extremely important for pulsed, high pressure discharges. To avoid the serration shape caused by Cartesian mesh generation, the immersed boundary method [42] was used in the Poisson equation.

The diagram of immersed boundary method is shown in figure 2. The white region represents the plasma, the blue region represents the ideal electrode area, and the red dashed line in the figure represents the actual electrode boundary. (x_1, y_1) and (x_2, y_2) are the intersection points of the line formed by the neighbor center points and point (i, j) with the electrode curve. We assume that the analytical formula for the shape of the electrode is $f(x, y) = 0$ and the voltage is V_b.

We use the middle points (red dots on the red dash lines in figure 2) at the interfaces between the plasma and the cathode

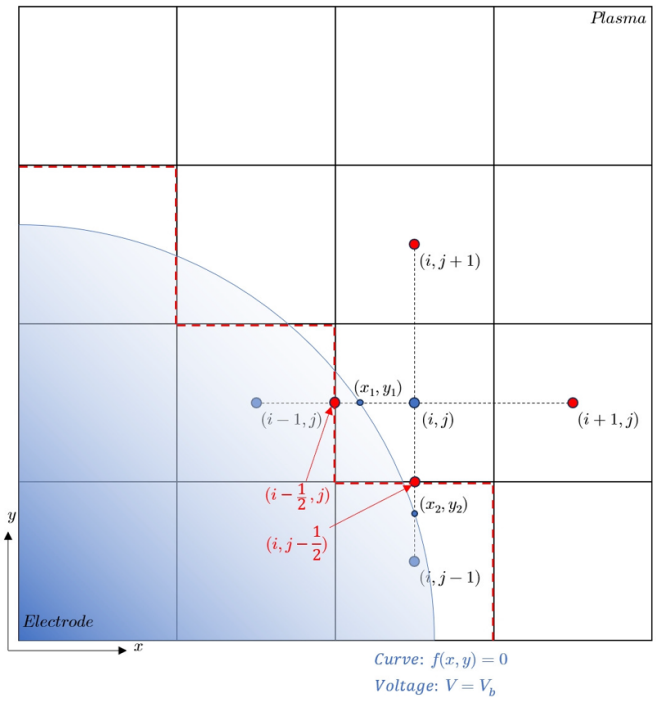

Figure 2. The diagram of Poisson equation discretion on the Cartesian grid.

to solve the Poisson equation, instead of point $(i-1,j)$ and point $(i,j-1)$. The discrete expression at point (i,j) is:

$$\alpha^E_{i,j}V_{i+1,j} + \alpha^W_{i,j}V_{i-1/2,j} + \alpha^S_{i,j}V_{i,j-1/2} + \alpha^N_{i,j}V_{i,j+1} + \alpha^C_{i,j}V_{i,j} = -\frac{\rho_{i,j}}{\varepsilon_0} \tag{13}$$

where α is the discrete coefficient of the equation, V is the voltage, $\rho_{i,j}$ is the charge at point (i,j).

The voltages of point (x_1,y_1) and point (x_2,y_2) are both V_b. Therefore, when the immersed boundary is applied, $V_{i-1/2,j}$ and $V_{i,j-1/2}$ can be linear interpolated. They can be expressed as a function of V_b, $V_{i,j}$ and the distance between them [43]. The discrete expression in the condition of immersed boundary is:

$$\alpha^E_{i,j}V_{i+1,j} + \alpha^{W'}_{i,j}V'_{i-1/2,j} + \alpha^{S'}_{i,j}V'_{i,j-1/2} + \alpha^N_{i,j}V_{i,j+1} + \alpha^C_{i,j}V_{i,j} = -\frac{\rho_{i,j}}{\varepsilon_0} \tag{14}$$

$$\frac{V'_{i-1/2,j} - V_b}{x_{i-1/2,j} - x_1} = \frac{V_{i,j} - V_b}{x_{i,j} - x_1} \tag{15}$$

$$\frac{V'_{i,j-1/2} - V_b}{y_{i,j-1/2} - y_2} = \frac{V_{i,j} - V_b}{y_{i,j} - y_2}. \tag{16}$$

The comparison of whether the immersion boundary is turned on or not is shown in figure 3.

Two types of BCs are usually selected in the plasma fluid model. The first one is the simple BC (continuity BC) that ignores the cathode sheath and secondary electron emission:

$$\boldsymbol{\Gamma}_e = -\mu_e n_e \boldsymbol{E} - D_e \nabla n_e \tag{17}$$

$$\boldsymbol{\Gamma}_{\text{ion}} = (q_{\text{ion}}/|q_{\text{ion}}|)\,\mu_{\text{ion}} n_{ion} \boldsymbol{E} - D_{\text{ion}} \nabla n_{\text{ion}} \tag{18}$$

$$\boldsymbol{\Gamma}_\epsilon = -\mu_\epsilon n_e \epsilon_m \boldsymbol{E} - D_\epsilon \nabla (n_e \epsilon_m). \tag{19}$$

Another BC is the physical BC, which calculates the secondary electron emission self-consistently. The emission of secondary electrons is related to the ion flux flowing in the boundary:

$$\boldsymbol{\Gamma}_e = \gamma \left(\sum_k \boldsymbol{\Gamma}_{\text{ion}} \right) \tag{20}$$

$$\boldsymbol{\Gamma}_{\text{ion}} = (q_{\text{ion}}/|q_{\text{ion}}|)\,\mu_{\text{ion}} n_{\text{ion}} \boldsymbol{E} - D_{\text{ion}} \nabla n_{\text{ion}} \tag{21}$$

$$\boldsymbol{\Gamma}_\epsilon = \gamma \left(\sum_k \boldsymbol{\Gamma}_{\text{ion}} \right) \cdot \epsilon_{\text{see}} \tag{22}$$

where $\boldsymbol{\Gamma}_e$, $\boldsymbol{\Gamma}_{\text{ion}}$ and $\boldsymbol{\Gamma}_\epsilon$ represent the boundary fluxes of electron, ion and electron energy, respectively. μ_e, μ_{ion} and μ_ϵ are the mobility of electron, ion and electron energy, respectively. n_e is the electron density, n_{ion} is the ion density and ϵ_m represents the mean electron energy. γ is the secondary electron emission coefficient, and ϵ_{see} is the mean electron energy of the secondary electron.

In the previous work, we attempted to simulate the sheath of plasma in the air at 1.0 atm. The results show that the mesh size near the cathode of the sheath needs to be smaller than 2.0 μm for analyzing the plasma in sheath [44]. Since the ArF excimer lasers works in high–pressure (3.4 atm in our model), there are the same difficulties when modeling it. In our previous calculations, it was found that regardless of the BCs used, the drift of the electron energy conservation equation always limits the time steps. If the simple BC is used, the maximum mean electron energy is about 5 eV, but if the physical BC is used, the maximum mean electron energy is about 11 eV near the sheath. The expression of $\triangle t$ is limited by Courant–Friedrichs–Lewy (CFL) condition:

$$\triangle t = \text{CFL} \cdot \frac{h}{\mu_\epsilon |\boldsymbol{E}|}. \tag{23}$$

We used BOLSIG+ [40] to calculate μ_ϵ, and represent μ_ϵ and $|\boldsymbol{E}|$ as functions of mean electron energy. When $\text{CFL} = 0.1$, $h = 3.9 \times 10^{-6}$ m, the diagram of $\triangle t$ changed with electron energy is shown in figure 4. It can be observed that when the maximum electron energy doubled, the time step has

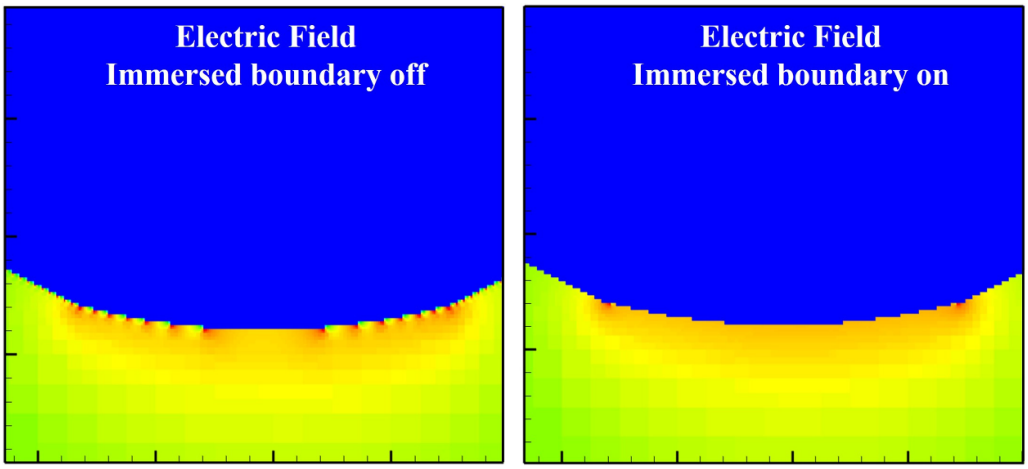

Figure 3. The comparison of electric field at the cathode tip when the immersed boundary is applied or not.

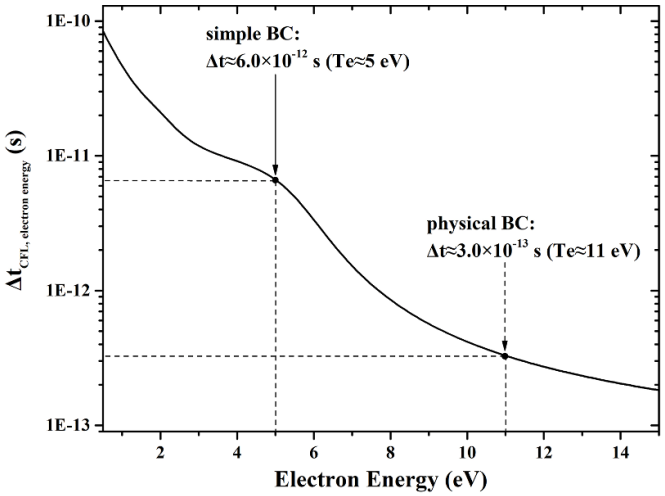

Figure 4. The simulation time step in different electron energy, calculated by BOLSIG+ [40]. The maximum electron energy in simple BC is 5 eV and the maximum electron energy in physical BC is 11 eV.

decreased by approximately 20 times. A long time step means that the time cost of using physical BC is too heavy in our model. Therefore, considering the time cost of calculation, we use the simple BC to calculate the discharge process.

In Xiong and Kushner's work [35], the eMCS was used to calculate the high–energy secondary electrons emitted from the cathode, and the important influence of high–energy electrons on the discharge current was evaluated. We have not yet implemented the function of electronic Monte–Carlo simulation in our model, so we try to apply an artificial BC to replace in phenomenology.

Specifically, we calculate the boundary fluxes under simple BC self–consistently at first, and then artificially increase the electron energy fluxes at the cathode boundary by a multiple coefficient k, that is:

$$\boldsymbol{\Gamma}_{\epsilon} = k \cdot \left(-\mu_{\epsilon} n_e \epsilon_m \boldsymbol{E} - D_{\epsilon} \nabla \left(n_e \epsilon_m\right)\right). \tag{24}$$

Table 1. List of plasma species.

Species	Name
Neutral species	Ar, F_2, Ne, Xe, F
Ar excited species	Ar^* (sum of 4 s), Ar^{**} (sum of 4p), Ar_2^*
Ne excited species	Ne^* (sum of 3 s), Ne_2^*
Dimer species	ArF^*, Ar_2F^*
Positive charged species	Ar^+, F_2^+, Ne^+, Xe^+, Ar_2^+, Ne_2^+
Negative charged species	F^-, e^-

In fact, the generation of high–energy electrons originates from the impact of ions on the cathode surface, and electrons are accelerated in the sheath. Based on this physical process, we multiply the electron energy flux by a coefficient k to replace the real high–energy electrons acceleration. While this configuration may not be entirely physically consistent or realistic, it allows us to capture the phenomenology. The parameters settings of the coefficient k in artificial BC is introduced below.

2.3. ArF plasma reactions

The reaction source term S_i reflects the changes caused by plasma reactions. S_i using a set of ODE equations to describe:

$$\frac{\mathrm{d}n_i}{\mathrm{d}t} = S_i = \sum_{j=1}^{j_{\max}} Q_{ij},\ j = 1,2,3,\ldots,j_{\max},\ i = 1,2,3,\ldots,N_{\text{total}}, \tag{25}$$

where j is the number of the reaction, i is the number of species, and Q_{ij} is the source term of species i from reaction j.

The simplified ArF reaction scheme considers four basic gas components: Ar, F_2, Ne, and Xe. The stoichiometric ratio (mole fraction) in the system is Ar/F_2/Ne/Xe = 0.035/0.001/0.96 399/0.00 001. The initial electron density is set to a small value $n_e = 10^6$ m^{-3} [45]. There are 44 plasma reactions involving 20 plasma species including electrons, excited state particles, positive ions, and negative ions are considered. Specific species are shown in table 1. The complete

Table 2. List of simplified plasma reactions.

No.	Equations	Rate Coefficient ($1\,s^{-1}$, $m^3\,s^{-1}$, $m^6\,s^{-1}$)	Reference
	1) Electron impact reactions		
1	$Ar + e \rightarrow Ar + e$	$f(\sigma)$	[46]
2	$Ne + e \rightarrow Ne + e$	$f(\sigma)$	[46]
3	$F_2 + e \rightarrow F_2 + e$	$f(\sigma)$	[46]
4	$Xe + e \rightarrow Xe + e$	$f(\sigma)$	[46]
5	$F_2 + e \rightarrow F^- + F$	$f(\sigma)$	[46]
6	$Ar + e \rightarrow Ar^* + e$	$f(\sigma)$	[46]
7	$Ar + e \rightarrow Ar^{**} + e$	$f(\sigma)$	[46]
8	$Ne + e \rightarrow Ne^* + e$	$f(\sigma)$	[46]
9	$F_2 + e \rightarrow F_2^+ + e + e$	$f(\sigma)$	[46]
10	$Ar + e \rightarrow Ar^+ + e + e$	$f(\sigma)$	[46]
11	$Ne + e \rightarrow Ne^+ + e + e$	$f(\sigma)$	[46]
12	$Xe + e \rightarrow Xe^+ + e + e$	$f(\sigma)$	[46]
	2) Stepwise ionization		
13	$Ar^* + e \rightarrow Ar^+ + e + e$	$f(\sigma)$	[46]
14	$Ne^* + e \rightarrow Ne^+ + e + e$	$f(\sigma)$	[46]
15	$Ar^{**} + e \rightarrow Ar^+ + e + e$	$1.56 \times 10^{-13}\,(T_e[eV])^{0.71} \exp(-2.63/T_e[eV])$	[20]
	3) Combination ionization/Penning ionization		
16	$Ne^* + Ar \rightarrow Ar^+ + Ne + e$	6.5×10^{-17}	[47]
17	$Ne_2^* + Ar \rightarrow Ar^+ + Ne + Ne + e$	6.5×10^{-17}	[47]
	4) Electron-ion recombination		
18	$Ar^+ + e \rightarrow Ar^{**}$	$4.0 \times 10^{-19}\,(T_e[eV])^{-0.5}$	[48]
19	$Ar^+ + e + e \rightarrow Ar^* + e$	$8.75 \times 10^{-39}\,(T_e[eV])^{-4.5}$	[49]
20	$Ar^+ + e + e \rightarrow Ar^{**} + e$	$5.0 \times 10^{-39}\,(T_e[eV])^{-4.5}$	[48]
21	$Ar^+ + e + Ar \rightarrow Ar^* + Ar$	1.0×10^{-38}	[50]
22	$Ar_2^+ + e \rightarrow Ar^* + Ar$	7.0×10^{-13}	[50]
	5) Electron impact de-excitation		
23	$ArF^* + e \rightarrow Ar + F + e$	2.0×10^{-13}	[51]
	6) Ion-Ion recombination		
24	$Ar^+ + F^- \rightarrow ArF^*$	1.0×10^{-12}	[52]
25	$F_2^+ + F^- \rightarrow F + F + F$	4.0×10^{-14}	[20]
26	$Ar_2^+ + F^- + M \rightarrow ArF^* + Ar + M$	$5.45 \times 10^{-11} \times N$	[47]
	7) Charge transfer		
27	$Ar^+ + Ar + Ne \rightarrow Ne^+ + Ar + Ar$	1.6×10^{-44}	[53]
28	$Ne^+ + Ar \rightarrow Ar^+ + Ne$	1.0×10^{-17}	[54]
29	$Ne^+ + Ne + Ne \rightarrow Ne_2^+ + Ne$	4.4×10^{-44}	[55]
30	$Ne_2^+ + Ne + Ar \rightarrow Ar^+ + Ne + Ne + Ne$	1.0×10^{-43}	[54]
31	$Ne_2^+ + Ar + Ar \rightarrow Ar^+ + Ne + Ne + Ar$	1.0×10^{-43}	[54]
	8) Two-body heavy particle reactions		
32	$Ar^* + F_2 \rightarrow ArF^* + F$	7.5×10^{-16}	[20]
33	$Ar^* + F_2 \rightarrow Ar + F + F$	3.1×10^{-16}	[20]
34	$Ar^{**} + Ar \rightarrow Ar^* + Ar$	1.0×10^{-16}	[20]
35	$Ar^{**} + F_2 \rightarrow ArF^* + F$	4.7×10^{-16}	[20]
36	$Ar^{**} + F_2 \rightarrow Ar + F + F$	3.1×10^{-16}	[20]
37	$ArF^* + Ar \rightarrow Ar + Ar + F$	9×10^{-18}	[20]
38	$ArF^* + F_2 \rightarrow Ar + F + F + F$	1.9×10^{-15}	[20]
39	$ArF^* + Ne \rightarrow Ar + F + Ne$	1.6×10^{-18}	[51]

(Continued.)

Table 2. (Continued.)

	9) Three-body heavy particle reactions		
40	$Ar^* + Ar + Ne \rightarrow Ar_2^* + Ne$	1.1×10^{-44}	[47]
41	$Ne^* + Ne + Ne \rightarrow Ne_2^* + Ne$	8.0×10^{-46}	[55]
42	$ArF^* + Ar + Ne \rightarrow Ar_2F^* + Ne$	3.5×10^{-43}	[20]
43	$ArF^* + Ne + Ne \rightarrow Ar + F + Ne + Ne$	1.0×10^{-44}	[20]
	10) Radiation reactions		
44	$ArF^* \rightarrow Ar + F$	2.5×10^{8}	[20]

plasma chemistry and simplifying strategy can be seen in the appendix.

2.4. Helmholtz photoionization model for ArF excimer lasers

Ultraviolet photoionization plays a significant role in self–triggering ArF excimer lasers, thereby influencing plasma propagation from the corona bar to the main gap. In this section, we discuss the treatment of photoionization in the numerical model.

The three–exponential Helmholtz model is used in this study, which has been previously suggested for quantifying the photoionization source term, denoted as S_{ph}:

$$S_{\mathrm{ph}}(\vec{r}) = \sum_j S_{\mathrm{ph}}^j(\vec{r}),\ j = 1,2,3. \tag{26}$$

$S_{\mathrm{ph}}^j(\vec{r})$ can be solved using Helmholtz equations:

$$\nabla^2 S_{\mathrm{ph}}^j(\vec{r}) - (\lambda_j p)^2 S_{\mathrm{ph}}^j(\vec{r}) = -A_j p^2 I_0(\vec{r}), \tag{27}$$

where λ_j and $A_j\,(j = 1,2,3)$ are fitting parameters for the equation, p is the gas pressure, $I_0(\vec{r})$ is the ionization source rate. The values of λ_j and A_j can be obtained by fitting the pressure-reduced photoionization rate function ψ_0/p. the expression of ψ_0/p is obtained from the work of Pancheshnyi [56]

$$\frac{\psi_0}{p} = (pr)\sum_j A_j \mathrm{e}^{-\lambda_j pr},\ j = 1,2,3, \tag{28}$$

$$\frac{\psi_0}{p} = \frac{p_q}{p+p_q}\frac{1}{4\pi}\frac{\omega}{\alpha_{\mathrm{eff}}}\frac{\int_{\lambda_{\min}}^{\lambda_{\max}} \xi_\lambda \left(\frac{\mu_\lambda}{p}\right) \mathrm{e}^{-\left(\frac{\mu_\lambda}{p}\right)pr} I_\lambda^0 \mathrm{d}\lambda}{\int_{\lambda_{\min}}^{\lambda_{\max}} I_\lambda^0 \mathrm{d}\lambda}, \tag{29}$$

where the term ψ_0/p can be divided into two parts:

$$\left(\frac{\psi_0}{p}\right)_{\text{strength}} = \frac{p_q}{p+p_q}\frac{1}{4\pi}\frac{\omega}{\alpha_{\mathrm{eff}}}, \tag{30}$$

$$\left(\frac{\psi_0}{p}\right)_{\text{distribution}} = \frac{\int_{\lambda_{\min}}^{\lambda_{\max}} \xi_\lambda \left(\frac{\mu_\lambda}{p}\right) \mathrm{e}^{-\left(\frac{\mu_\lambda}{p}\right)pr} I_\lambda^0 \mathrm{d}\lambda}{\int_{\lambda_{\min}}^{\lambda_{\max}} I_\lambda^0 \mathrm{d}\lambda}, \tag{31}$$

where p_q is the quenching pressure of the emitting gas, ω is the excitation coefficient of emitting states, α_{eff} is the effective Townsend coefficient, $(\lambda_{\min}, \lambda_{\max})$ is the spectral range of the radiation, ξ_λ and μ_λ are the spectrally resolved photoionization yield and the absorption coefficient, respectively, and I_λ^0 is the spectral density of ionizing radiation

$$\xi_\lambda = \frac{\sigma_{\text{ionization}}(\lambda)}{\sigma_{\text{absoption}}(\lambda)}, \tag{32}$$

$$\frac{\mu_\lambda}{p} = \frac{\sigma_{\text{absoption}}(\lambda)}{k_b T}. \tag{33}$$

Specifically, in ArF excimer lasers model, the photoionization radiation comes from the 85 nm UV–light emitted by Ne_2^*, and the ionized specie is Xe, because Xe has the lowest ionization threshold in the gas mixture (Ar: 15.76 eV, F_2: 15.69 eV, Ne: 21.65 eV, Xe: 12.13 eV). It has been reported that adding Xe (even at partial pressure of less than 0.1 Torr) into Ar/F_2/Ne mixtures sharply increases the photo–charge signal in the experiment. Similar conclusions have been drawn in a study of XeF excimer lasers [57]. Besides, the reason why we choose this process is based on the work of Xiong and Kushner [35], it is believed that the conversion rate from Ne^* to Ne_2^* is quite fast at high gas pressures. Xiong mentioned that although there may be other photoionization processes and radiation sources during the discharge of gas mixtures, this choice represents general scaling laws of photo triggered discharges.

Mimicking the equations mentioned above, the photoionization function of Xe–Ne can be written is shown following form:

$$\left(\frac{\psi_0}{p}\right)_{\text{Xe,Ne}} = \eta_{\mathrm{Xe}}\left(\frac{p_q}{p+p_q}\right)_{\text{Xe, Ne}}\frac{1}{4\pi}\left(\frac{\omega}{\alpha_{\mathrm{eff}}}\right)_{\text{Xe, Ne}} \cdot \frac{\int_{\lambda_{\min}}^{\lambda_{\max}} \xi_{\lambda,\mathrm{Xe}} \left(\frac{\mu_{\lambda,Xe}}{p}\right) \mathrm{e}^{-\left(\frac{\mu_{\lambda,\mathrm{Xe,Ne}}}{p}\right)pr} I_{\lambda,\mathrm{Ne}}^0 \mathrm{d}\lambda}{\int_{\lambda_{\min}}^{\lambda_{\max}} I_{\lambda,\mathrm{Ne}}^0 \mathrm{d}\lambda}, \tag{34}$$

$$\mu_{\lambda,\mathrm{Xe,Ne}} = \eta_{\mathrm{Xe}} \cdot \mu_{\lambda,\mathrm{Xe}} + \eta_{\mathrm{Ne}} \cdot \mu_{\lambda,\mathrm{Ne}}. \tag{35}$$

Due to the absence of experimental photoionization data for validation, the distribution function of photoionization is the first to be solved. The photoabsorption cross sections, absorption coefficients of Ne and Xe, and the emission spectrum of Ne are shown in figure 5.

It should be noted that (1) the photoabsorption cross section of Ne lacks data between 12.1 $\sim$ 16 eV (77.5 nm $\sim$ 102 nm), so we assumed its absorption coefficients to be low ($10^{-5}\,\mathrm{cm}^{-1}\cdot\mathrm{Torr}^{-1}$). (2) The ultraviolet emission spectrum of

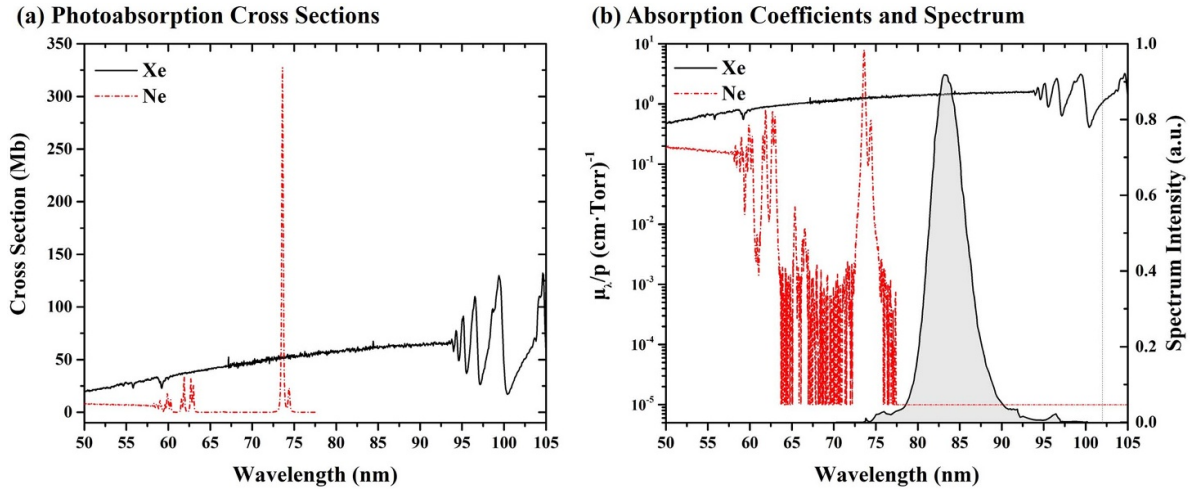

Figure 5. (a) The photoabsorption cross sections of Xe (black solid line)and Ne (red dash-dotted line), and the data are from Chan *et al* [58, 59]. (b) The emission spectrum of Ne at 1.2 atm (filled line), and the data are from Morozov *et al* [60].

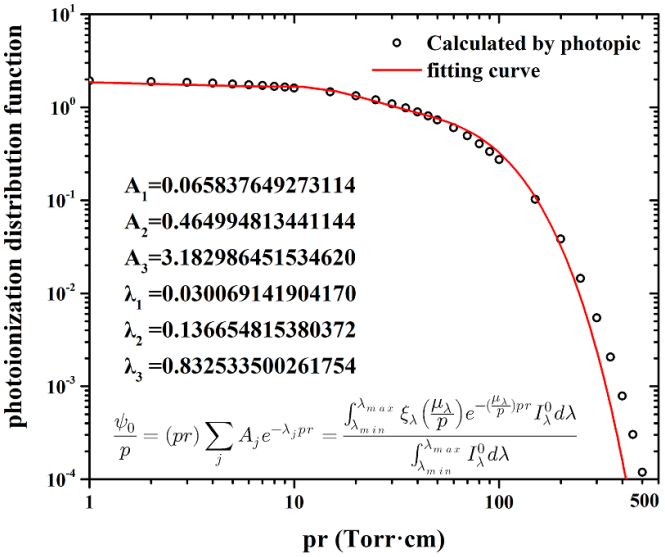

Figure 6. The photoionization distribution function calculated by PHOTOPiC (black points) and fitting curve (red line), and the fitting data are shown in the blank.

Ne was measured at 1.2 atm instead of higher pressure due to a lack of relevant data. (3) The current photoionization model has limitations. The using model contains the absorption properties of the photons (optically thick), but the emission from Ne_2^* is usually considered as optically thin.

In the current model, I_λ^0 is the emission spectrum density of Ne_2^*. The real ultraviolet radiation emitted by Ne_2^* is stronger compared to the calculated results due to the lack of resonance trapping. The photoionization distribution function is solved using a well–validated online tool PHOTOPiC [61], and the three–exponential terms are fitted using the Nelder–Mead Simplex Direct Search method. The results are shown in figure 6.

After the photoionization distribution function confirmed, here, the photoionization strength references the work of Xiong and Kushner in 2010 [34]. This is because the ionizing radiation comes from Ne_2^* has a nonlinear relationship with direct excitation of the monomer. When the excitation rate is directly related to the photon emission such as O_2, N_2, etc the photoionization intensity should satisfy [62]:

$$I_0(\vec{r}) = \xi \frac{n_u(\vec{r})}{\tau_u} = \xi \frac{p_q}{p + p_q} S_i(\vec{r}), \tag{36}$$

where ξ is the efficiency of photoionization, $n_u(\vec{r})$ is the density of excited species, τ_u is the radiative lifetime of excited species, p_q is the quenching pressure, $S_i(\vec{r})$ is the source term of ionization. We further simplify the above equation by directly correlating $I_0(\vec{r})$ with $S_i(\vec{r})$ instead of considering the linear relationship, and determine the proportion coefficient from the published literature, i.e.:

$$I_0(\vec{r}) = \eta \cdot S_i(\vec{r}) \tag{37}$$

η is determined by the work published by Xiong and Kushner [34]. In their model, The photoionization intensity $I_0(\vec{r})$ is indeed directly calculated from the density of excited species Ne_2^* , and the results showed that the photoionization source term is about one thousandth of the ionization source term (figures 5(a) and (d) in the reference), so we will adjust the coefficient η set to 0.001. Therefore, the intensity of photoionization can be characterize by employing an approximate coefficient. Although the nonlinear relationship between excitation rate and photoelectric emission does indeed affect the accuracy of the model, the coefficient η can ensure that the strength of photoionization is within a reasonable range.

2.5. The external circuit model

When coupling external circuits, only the time domain transient state can be analyzed due to the plasma acting as a non–linear black box. The external circuits module solves the ODEs in the time domain to obtain the circuit voltages and currents timely, and transport the circuit data as the BC of the Poisson

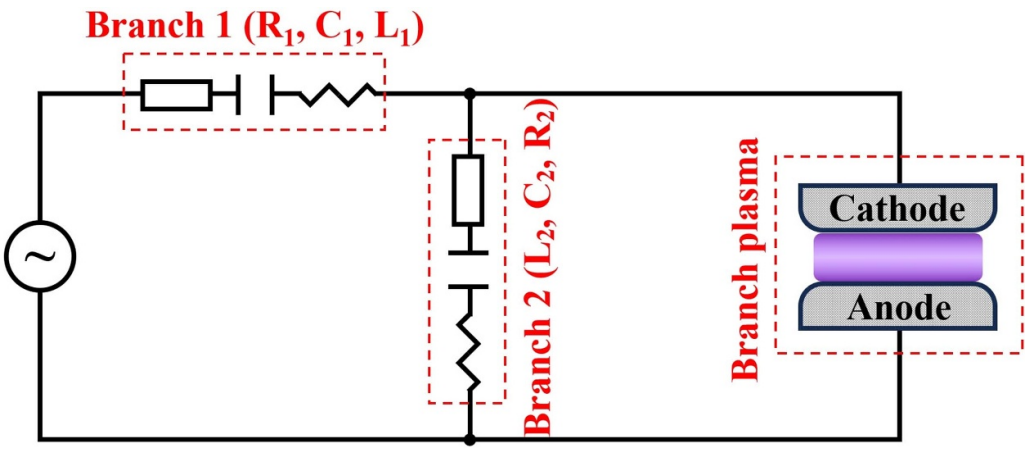

Figure 7. The diagram of external circuit.

Table 3. Short circuit/open circuit assignment for each branch circuit component.

Circuit element type	Short circuit	Open circuit
Resistor	$R = 0$ (0 Ω in practice)	$R = \infty$ (10^{9} Ω in practice)
Capacitor	$C = \infty$ (10^{9} F in practice)	$C = 0$ (10^{-14} F in practice)
Inductor	$L = 0$ (10^{-20} H in practice)	$L = \infty$ (10^{9} H in practice)

equation to the plasma module. The electrode current can be divided into two parts, the displacement current and the conduction current. The conduction current is obtained by integrating the fluxes of various charged species on the electrode surface, while the displacement current is the integration of the derivative of the potential displacement vector over time on the electrode surface

$$I = \int_{\text{electrode}} \left(\sum\nolimits_i q_i \phi_i + \frac{\mathrm{d}(\varepsilon \boldsymbol{E})}{\mathrm{d}t} \right) \cdot \hat{n} \mathrm{d}A. \tag{38}$$

A simplified external circuit of ArF excimer lasers and adjustable parameters are shown in figure 7. Two RLC branches and the voltage source were set up. The assignment of circuit components in the short circuit and the open circuit branch can be referred to in table 3. The circuit model can be equivalent to a zero input response with the voltage source set to 0. Capacitor C_1 has a initial voltage. Capacitor C_2 is charged rapidly to increase the voltage.

3. Result and Discussion

3.1. Discharge evolution in one single pulse of ArF excimer lasers

The electron density spatial distribution is shown in figure 8 at times 30, 50, 65 and 76 ns. These four typical figures represent the discharge inception, propagation, and breakdown in a single pulse.

Firstly, at 30 ns, the discharge initiates from the contact point between the cathode and the corona bar, generating surface streamers in both clockwise and counterclockwise directions. The electrons subsequently occur in the small gap between the cathode and the corona bar, merging with the surface discharge. The surface streamer propagates at an average speed of 2×10^{8} cm s^{-1} and has a thickness of 0.5 mm. The electron density in the streamer reaches 10^{19} m^{-3}.

Secondly, photo–generated electrons propagate from the corona bar surface to the main gap. At 65 ns, the electron density between the main gap reaches 10^{15} m^{-3} , and the plasma generated from the cathode and the anode develops in opposite directions. Notably, different from the narrow, thin, and streamer–like shape of plasma shown in Xiong's work (figure 5 in [35]), the photo–generated electrons during propagation are uniform and disperse in our computation. This difference in electron density distribution may be caused by the distinct input parameters of the photoionization model. Moreover, there is a low electron density region near the cathode surface as depicted in figure 8(c). The electrons are pushed away due to the electric field being perpendicular to the cathode surface. Neglecting the high–energy secondary electron emission in the model is another reason for causing the electron density blank near the cathode.

Thirdly, at 76 ns, the electron density of 10^{18} m^{-3} completely filled the main gap for the first time. Due to the effect of photoionization, the plasma is asymmetric. The plasma on the right side of axis AB is wider. When the electron density reaches 10^{18} m^{-3} for the first time, we define this moment as the breakdown time, since the current will increase steeply soon after as shown in figure 9(a). Meanwhile, the U_{gap} is no longer equal to U_{C2} because based on Kirchhoff's Law, U_{C2} can be written by the following equation:

$$U_{C2} = U_{L2} + U_{\text{gap}}, \tag{39}$$

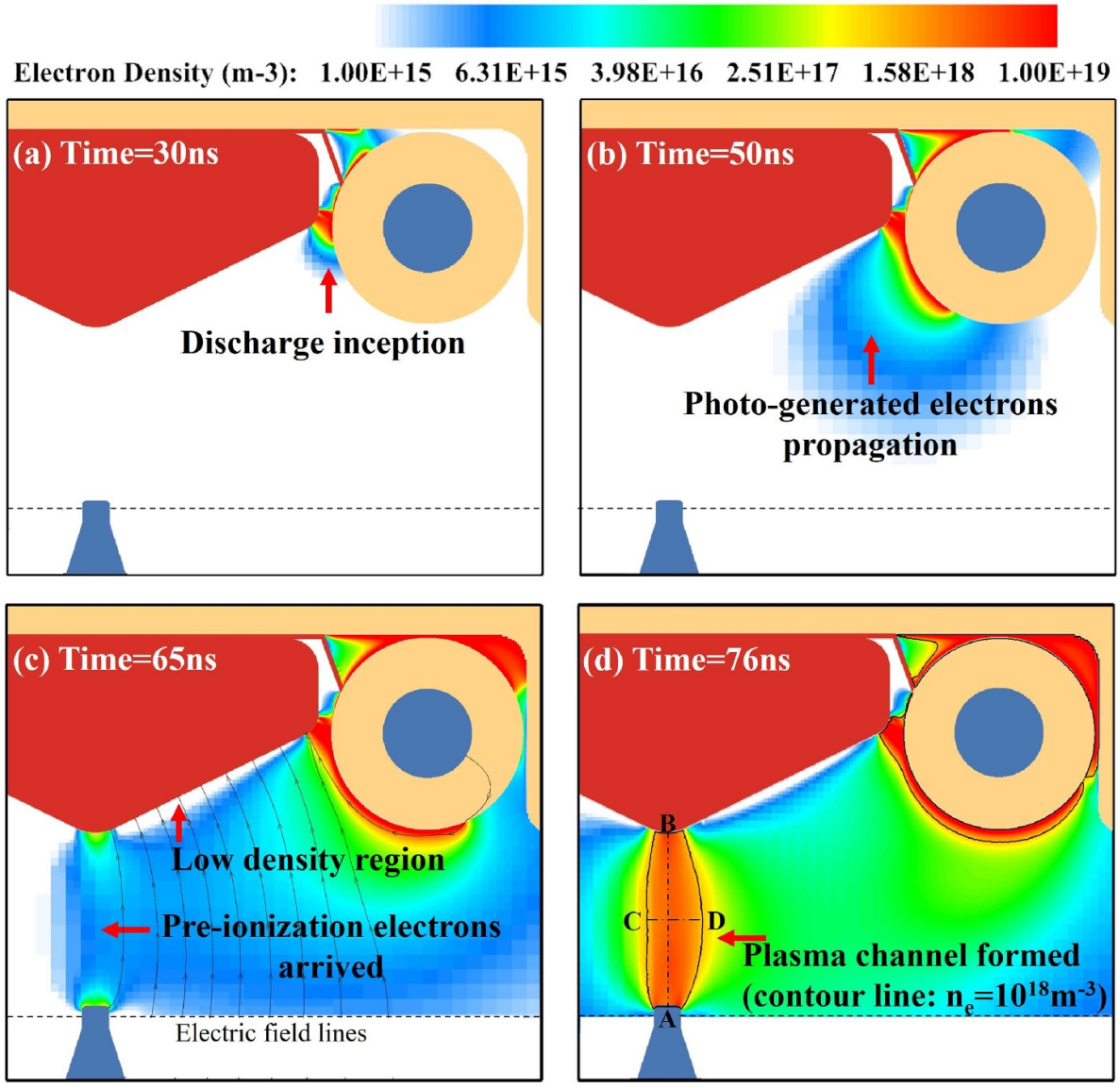

Figure 8. The electron density distribution (n_e) at (a) 30 ns, (b) 50 ns, (c) 65 ns, (d) 76 ns, unit in m^{-3}, and partial electric field lines at 65 ns.

where U_{L2} is the voltage of inductor L_2, and $U_{L2} = L_2 \cdot \mathrm{d}I/\mathrm{d}t$. Therefore, the U_{L2} is not equal to zero when the current increased.

The comparison of the experimental voltages and calculated voltages is shown in figure 9(b). Both U_{C1} and U_{C2} are consistent in changing trends. The peak–to–peak voltage calculated as $((\Delta U_{\mathrm{sim}} - \Delta U_{\mathrm{exp}})/(\Delta U_{\mathrm{exp}}))$ has a relative error of 4.2%. The voltage turning point time has a relative error of 7.0%.

We suspect the delay in the turning point and the reduction in the peak–to–peak voltage are attributed to neglecting the impact of high–energy electron emission. It has been reported that runaway electrons can accelerate plasma propagation [63], leading to an advancement in breakdown time. Besides, the sheath–accelerated electrons emitted from cathode are critical to the discharge current [35], and the discharge current will affect the rising of the reverse voltage. To confirm the aforementioned view, the work applying the artificial BC to characterize high–energy electrons emission will be introduced in next section.

3.2. *The influence of surface discharge propagation along the cathode*

As mentioned in section 2.2, the expression for the electron energy boundary flux on the cathode surface is defined by equation (24) when the artificial BC is activated. We set $k = 200$ based on previous parameterized calculations and empirical knowledge. When the artificial BC is applied, the electron energy flux at the cathode boundary will be calculated self–consistently firstly, then the flux is multiplied by k.

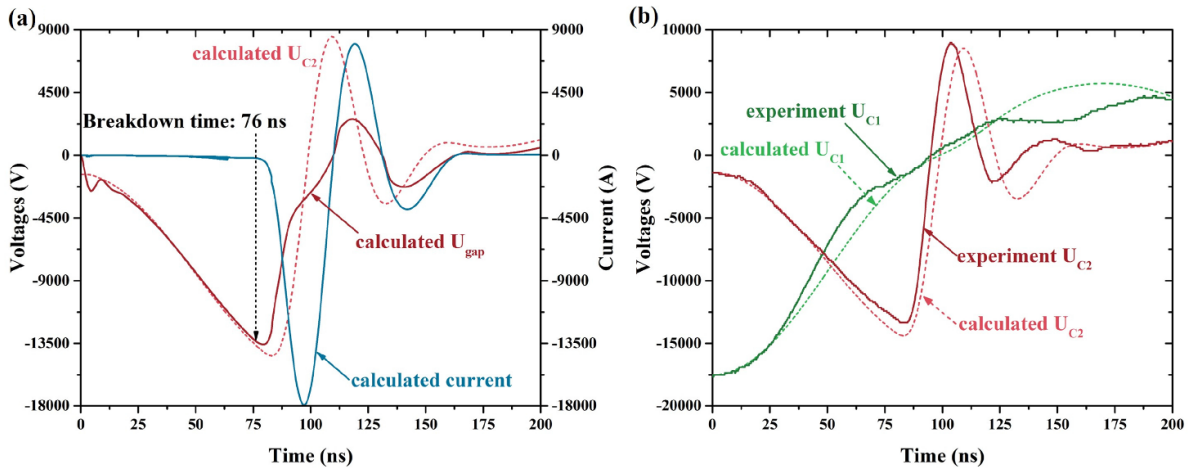

Figure 9. Only considering the photoionization: (a) the voltage of the cathode (U_{gap}), capacitor C_2 (U_{C2}) and the plasma current, (b) the experimental and calculated voltages of capacitor C_1 (U_{C1}) and capacitor C_2 (U_{C2}).

As depicted in figure 10, the artificially increased electron energy flux elevates the electron temperature on the cathode surface, reaching a maximum value of approximately 55 000 K. Compared to the simple BC, applying the artificial BC is a phenomenological effect for simulating the surface ionization on the cathode surface, similar to the surface streamer head on the surface of the corona bar. When the electron density on the surface reaches 10^{15} m^{-3}, the artificial BC reverts to the simple BC to prevent the uncontrolled growth of electrons.

The electron density spatial distribution is shown in figure 11 at 30, 50, 62 and 73 ns, with the first three figures corresponding to the timestamps in figure 8.

At 30 ns, different from figure 8(a), the artificial surface discharge initiates from the small gap between the cathode and the corona bar. Then, at 50 ns,the electron density increases on the cathode surface as volumetrically photo–generated electrons propagate, filling the local low electron density region near the cathode surface. The propagation speed of artificial surface discharge is approximately 3.7×10^7 cm s^{-1}, determined by the multiplication coefficient k. The thickness of the surface plasma is about 0.1 mm. Both the thickness and the speed are smaller and slower than those of a classical surface streamer.

At 62 ns, compared to figure 8(c), the discharge propagation near the cathode accelerates. The breakdown time occurs 3 ns earlier than in the normal photoionization case due to the cathode surface discharge. Next, a symmetric plasma channel was formed at 73 ns.

Changes in electrical parameters and density of key species reflect the effects caused by applying the artificial BC. The cathode voltage and plasma current are shown in figure 12(a). It can be observed in figure 12(b) that species distribution along line CD is more uniform when the artificial BC is effective, and the average density of n_e and ArF* is higher. Figure 12(a) also shows that the turning time of gap voltage advanced. Although the turning point time is advanced, applying the artificial BC cannot make key species densities increasing significantly in the main gap. The increase in electron energy at the cathode surface is temporary due to the electron density has been lager than 10^{15} m^{-3} when the main discharge started. Therefore, different from eMCS, there is no high–energy electron emission when the discharge propagates between the main gap, as the plasma is calculated self–consistently without applying the artificial BC.

Considering the discussions on the morphology of plasma during propagation in sections 3.1 and 3.2, in order to confirm the characteristics of plasma propagation, a simple ICCD images experiment was conducted. The position relationship between the camera and the discharge chamber is shown in figure 13(a). An ICCD camera was used to capture images from the side of the discharge chamber, with a pulse trigger controlling the camera's triggering time and adjusting the relative timing between the camera shutter and the experimental voltage, as shown in figure 13(b). The gate width of the ICCD camera was set to 5 ns.

Due to the size limitation of the observation window, the camera can only capture the bottom of the corona bar and the main discharge gap. As shown in figure 13(c), it can be seen that the luminescence area at the bottom surface of the corona bar existed for at least 20 ns. However, there was always a dark area between the bottom of the corona bar and the cathode, even though the main discharge has been observed in the last trigger image, inferring that plasma propagation is not observed along the cathode surface. It is concluded that there might be no obvious discharge phenomenon in this area.

3.3. A comparison of background electron density and photoionization

To further explore the unique effect of photoionization, a comparison case of high–level background electron density was computed. The background electron density was set to be 10^{15} m^{-3} initially corresponding to the photo–generated electron density reaches 10^{15} m^{-3}.

The electron density spatial distribution is shown in figure 14 at 25, 45, 65 and 72 ns with the first three figures corresponding to the timestamps in figure 8.

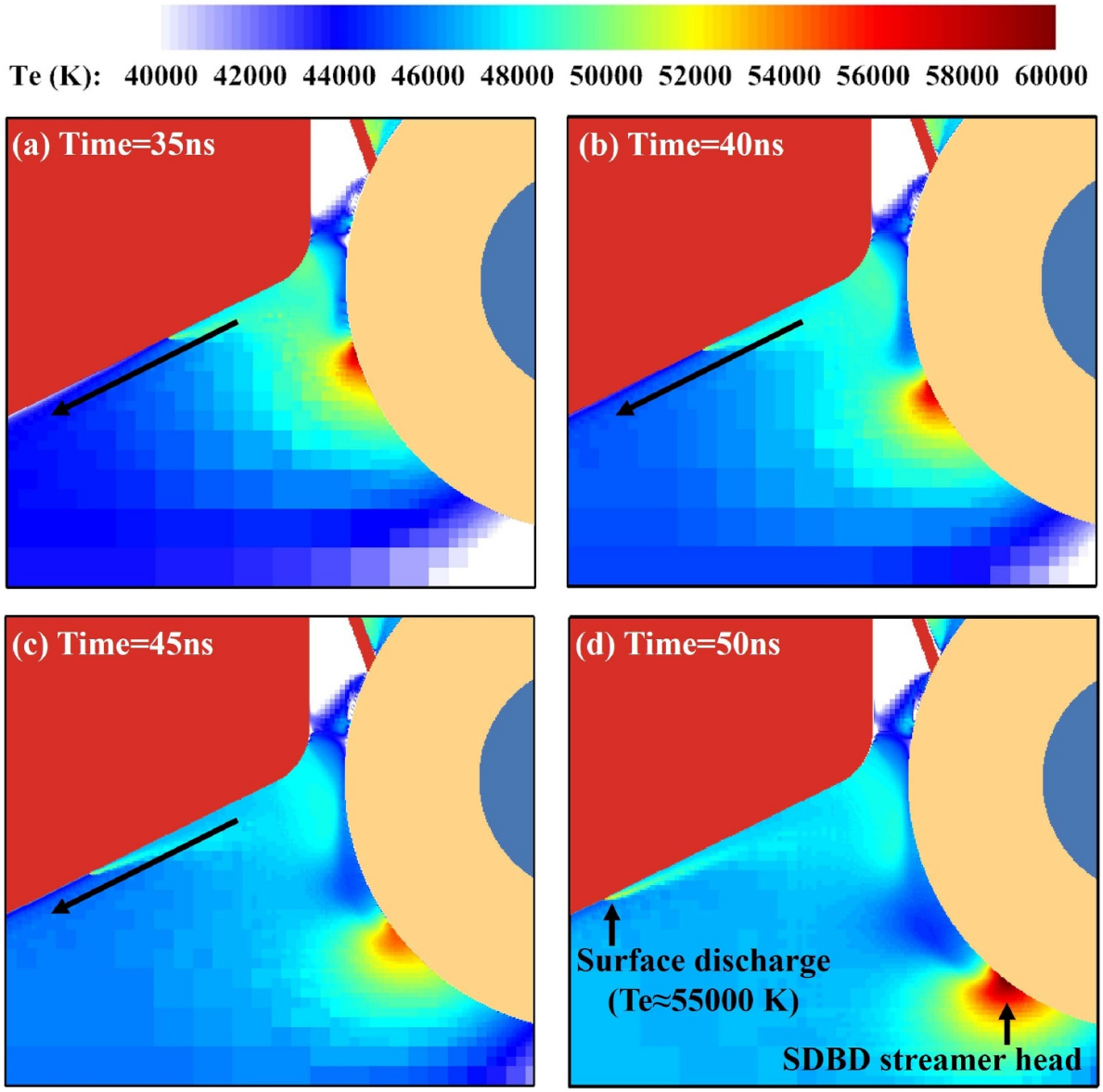

Figure 10. The electron energy distribution (T_e) at (a) 35 ns, (b) 40 ns, (c) 45 ns, (d) 50 ns, unit in K. The artificial BC is applied, and the long black arrow represents the direction of surface discharge.

Firstly, the discharge evolution is distinct in the two cases. At 30 ns, the inception of discharge around the corona bar was observed, with no difference in discharge inception between the background ionization case and the photoionization case. However, at 45 ns, the discharge did not propagate from the corona bar to the main gap. The main discharge time was advanced due to the sufficient background ionization density in the main gap. At 72 ns, the plasma channel formed 4 ns earlier compared to the photoionization situation. The time advance of breakdown can be observed from the electron density in figure 14(d). The uniformity of discharge has improved, and the electron density distribution on both sides of axis AB is nearly symmetrical.

Secondly, electrical parameters and species densities are distinct in two cases. The comparison of U_{C2} is shown in figure 15. The relative error between the two cases and the experimental measurement of U_{C2} is small in both cases. It can be seen that the turning time of U_{C2} in the photoionization case is slightly later than in the case with uniform 10^{15} m^{-3} background ionization. The discharge voltage, current and key species densities of two cases are shown in figure 16. Comparing the circuit parameters and species densities, it can be observed that the current is higher, but the electron density and ArF^* density are lower when photoionization is turned on.

The reason for the aforementioned phenomenon is the constant presence of a 10^{15} m^{-3} background ionization inside the discharge chamber. While self–consistent photoionization can also achieve a 10^{15} m^{-3} electron density, the discharge has to gradually propagate to the main gap. The background ionization acts as an independent pre–ionization, similar to X–rays. Therefore, if background ionization is used to model discharges in excimer lasers instead photoionization, the effect of

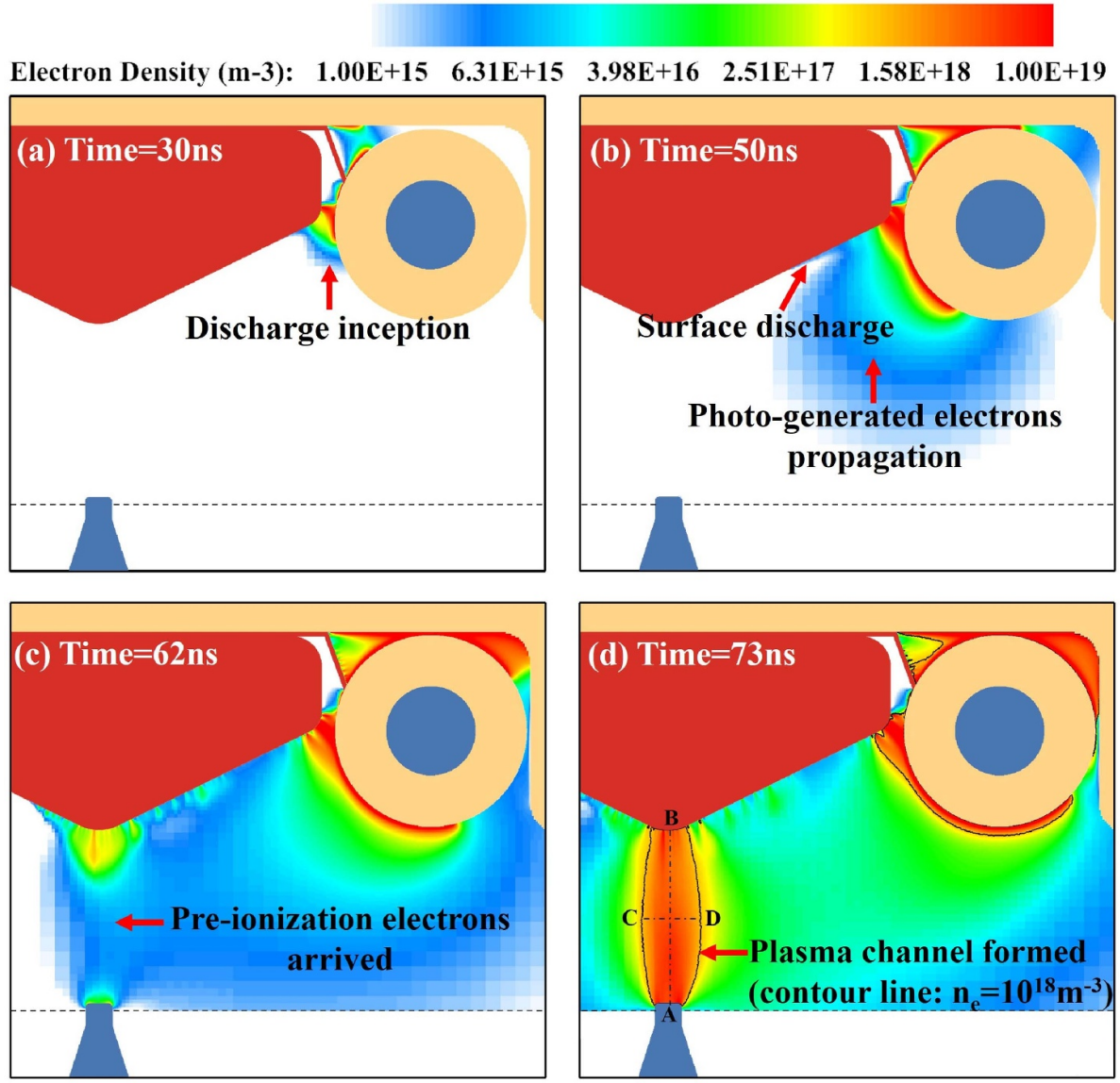

Figure 11. The electron density distribution at (a) 30 ns, (b) 50 ns, (c) 62 ns, (d) 73 ns, unit in m^{-3}. Both the photoionization and the artificial BC turned on.

pre–ionization may be overestimated. Photoionization can be replaced by background ionization in a single–pulse discharge if the electron density growth during the propagation process is neglected. However, further research is needed to investigate the replaceability of pre–ionization conditions under high–frequency discharge.

4. Conclusions

In summary, the pre–ionization in ArF excimer lasers has been investigated computationally in this work using a 2D plasma simulation code, *PASSKEy*. A set of simplified plasma reactions was summarized from the complete plasma reactions sensitivity analysis. The three-exponential Helmholtz model was adopted to describe the photoionization in the ArF excimer laser discharge. Input parameters of photoionization model were retrieved in detail. The spatial–temporal evolution of plasma was computed and discussed. Besides, an experiment was conducted to diagnose the morphology of plasma propagation from the corona bar to the main gap. It is found that there is no obvious discharge on the side of cathode surface.

(1) In the numerical model, the spatial–temporal evolution of electron density showed the discharge inception, propagation and breakdown clearly. The calculated voltage parameters match well with the experimental measurements. The relative error of peak–to–peak voltage is about 4.2% and the relative error of voltage turning time is about 7.0%. It is notable that the shape of plasma is uniform and dispersed when propagating from the corona bar to the main gap. The photo–generated electron density achieved 10^{15} m^{-3}. Affected by electric field direction, the plasma density on the cathode surface is lower than 10^{15} m^{-3} when plasma propagating. Due

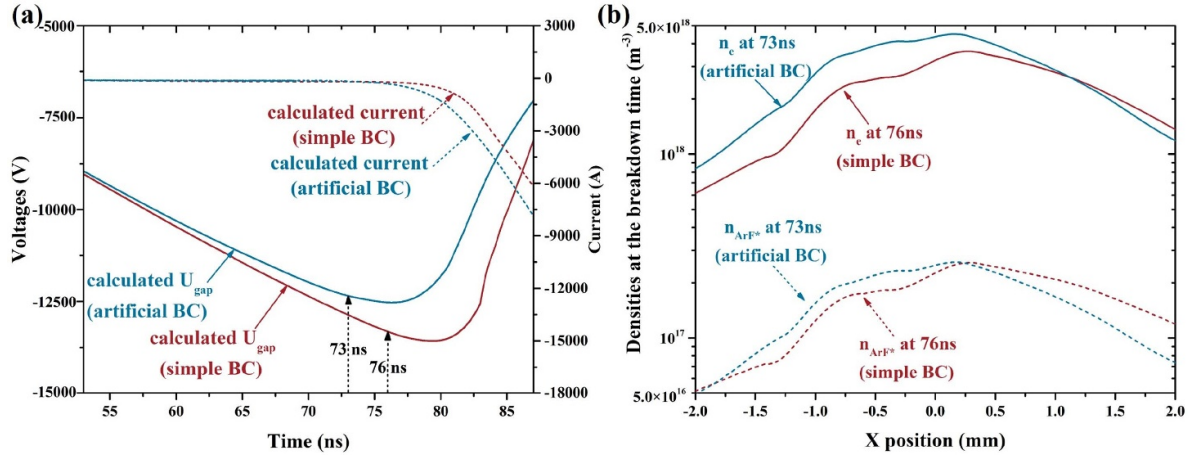

Figure 12. Comparisons of electrical parameters between the simple BC case and the artificial case. (a) The cathode voltage and plasma current. (b) The electron and ArF^* density distribution on line CD at the breakdown time (76 ns in the simple BC case and 73 ns in the artificial BC case).

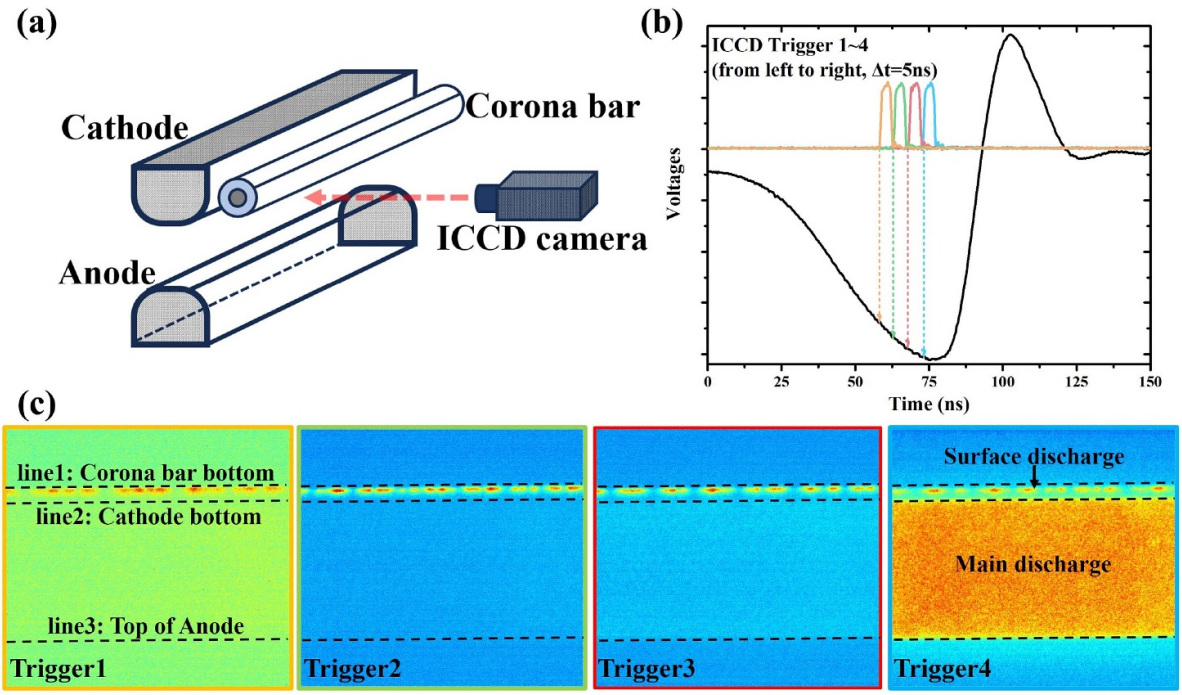

Figure 13. (a) The diagram of the relative position between the ICCD camera and the discharge chamber, (b) the relative time between ICCD camera and discharge voltage U_{C2}, (c) ICCD images corresponding to four trigger times.

to the single placement of the corona bar, photoelectrons are provided on only one side, causing the plasma morphology to exhibit asymmetry.

(2) In order to investigate the role of cathode surface emitted electrons in plasma propagation, an artificial BC is applied to replace the eMCS in phenomenology. The simulation results show that the artificial BC provides a surface ionization source. The plasma generated from the cathode surface advanced the breakdown time, and eliminated the asymmetry of plasma channel caused by photoionization. The ICCD images showed the dark region between the cathode bottom and the corona bar, where represents the side of the cathode surface. It is believed that photoionization is the dominant propagation mechanism, rather than high–energy electron emission.

(3) Finally, a comparison between the photoionization and a 10^{15} m^{-3} background ionization was made. It is found that the 10^{15} m^{-3} background ionization cannot lead the plasma propagation between the corona bar to the main gap. The surface discharge along the corona bar and the volumetric discharge in the main gap are independent. For one single pulse discharge in the main gap, the results reveal that the photoionization can be replaced by the background ionization in one single pulse discharge.

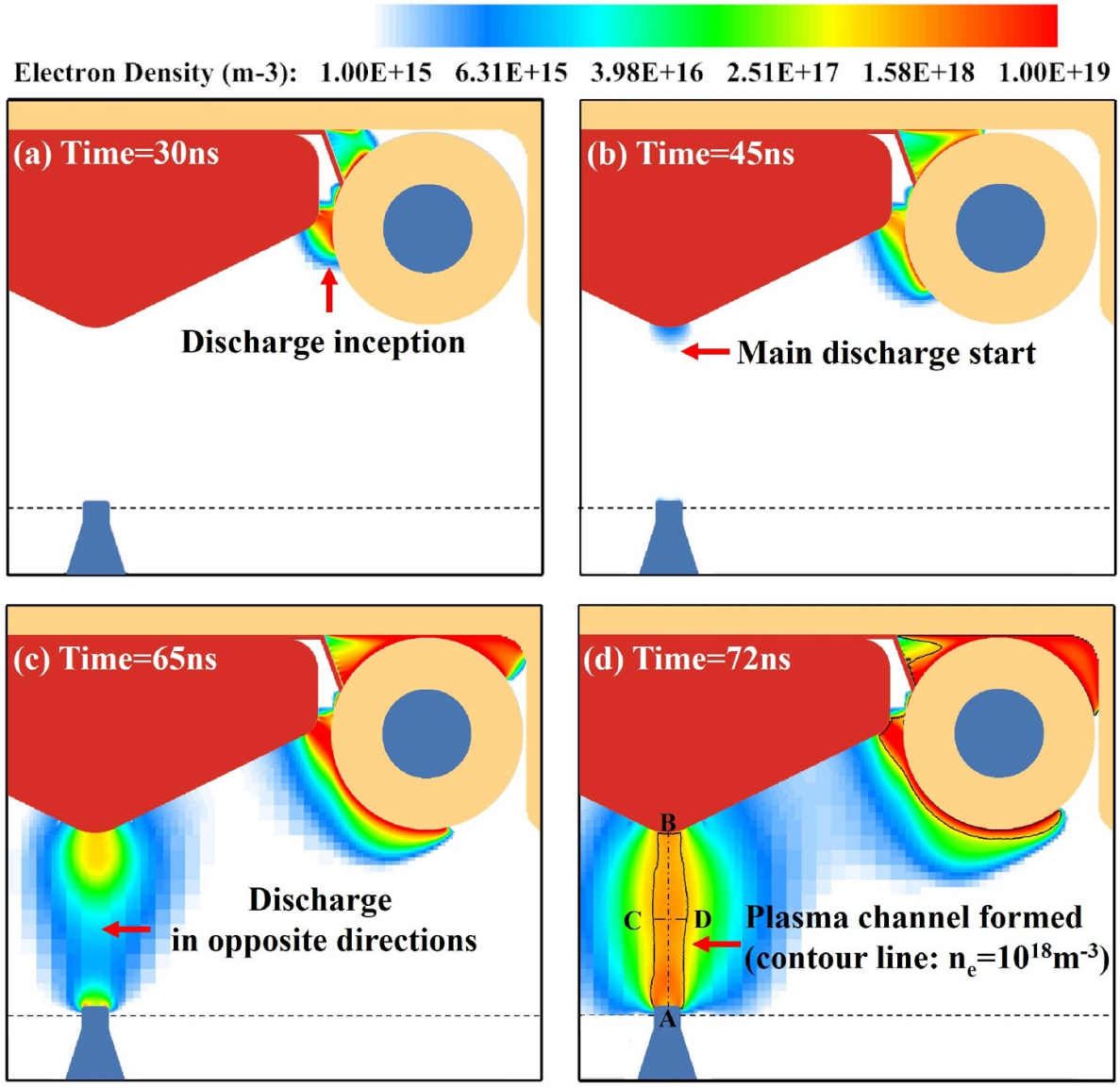

Figure 14. The electron density distribution at (a) 30 ns, (b) 45 ns, (c) 65 ns, (d) 72 ns, unit in m^{-3}. The initial background electron density is 10^{15} m^{-3} with photoionization off.

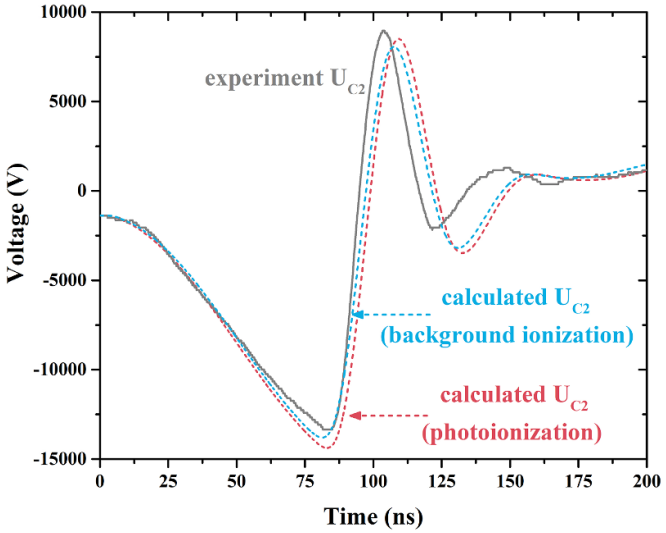

Figure 15. Comparisons of electrical parameters U_{C2} between the photoionization case and the background ionization case.

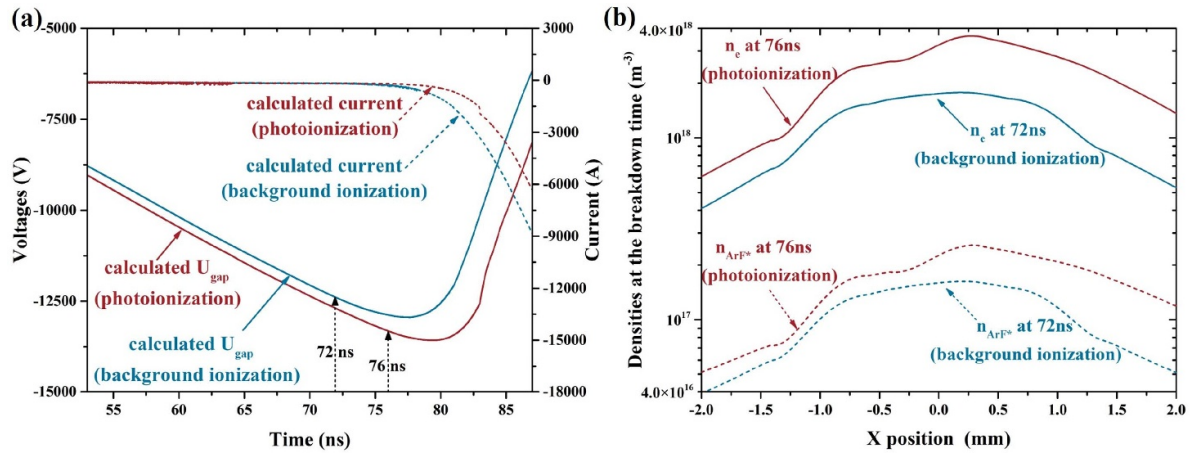

Figure 16. (a) Comparisons of the cathode voltage and plasma current between the photoionization case and the background ionization case. (b) The electron and ArF* density distribution on line CD at the breakdown time (76 ns in photoionization case and 72 ns in background ionization case).

Data availability statement

The data cannot be made publicly available upon publication because they contain commercially sensitive information. The data that support the findings of this study are available upon reasonable request from the authors.

Acknowledgments

The work is supported by the National Key Research and Development Program of China (2022YFC2604002), National Natural Science Foundation of China (Nos. 52277168, 52025064 and 92271113). The authors thank the young research group in Atelier des Plasmas for fruitful discussions and the Gongfang Tech Co, Ltd for technical support.

The authors thank prof. Zheng Zhao and Mr. Qiuyu Gao from Xi'an Jiaotong University for their great help in the experiment of this work.

Appendix. The ArF plasma chemistry and simplifying strategy

The complete ArF reaction scheme considers 152 plasma reactions involving 28 plasma species including electrons, excited state particles, positive ions, and negative ions. Specific species are listed in table 4. Electron collision reaction rates considering the superelastic collision in the reaction system are calculated using BOLSIG+ [40]. Lumped cross sections are employed to reduce the number of excited states. Cross–section data for Ar, Ne, and Xe are obtained from the Puech Database, while cross–section data for F_2 are obtained from the SIGLO Database. Table 5 shows the entire plasma reactions and their rate coefficients.

Due to the large number of species in the complete plasma reaction system, a 0D sensitivity analysis is employed to simplify the mechanism, enabling it to be conducted within an acceptable computational burden for two–dimensional simulations. The sensitivity analysis determines the importance of reactions by sequentially 'deleting' each reaction and evaluating the relative changes in electron and ArF* densities. The sensitivity coefficient is defined as follows [64]:

$$\phi(t)_{i,r} = \frac{n_{i,r=0}(t) - n_{i,r}(t)}{n_{i,r}(t)} \tag{40}$$

where r is a reactions rate for the ith reaction, $n_{i,r=0}(t)$ and $n_{i,r}(t)$ are the densities of the component under study with modified and no–modified rates, respectively. The threshold of 'important' was set by the following condition for any time instant t:

$$|\phi(t)_{i,r}| \geqslant 0.01. \tag{41}$$

The reduced electric field (E/N) inputs used for sensitivity analysis are 0 Td, 5 Td, 10 Td, and 15 Td, each with a duration of 50 ns. These E/N values cover the magnitudes present during most of a single pulse discharge. The E/N inputs for validating the simplified chemistry are obtained from the evolution of the computed E/N at the center position of the main gap in a single–pulse discharge, which is calculated in the preliminary computations. The simplified plasma chemistry is shown in table 2, and the comparison between complete chemistry and simplified chemistry is shown in figure 17.

It should be emphasized that the simplified plasma chemistry is only applicable for modeling discharge during propagation and breakdown. In the later stage of discharge channel formation, differences in electron density and excited species density appear when comparing the simplified and complete mechanisms. Therefore, for multiple or longer–duration discharges, the simplified plasma reactions will no longer be applicable, and a more comprehensive reaction mechanism should be considered.

Table 4. List of plasma species.

Species	Name
Neutral species	Ar, F_2, Ne, Xe, F
Ar excited species	Ar^* (sum of 4 s state), Ar^{**} (sum of 4p state), Ar_2^*
Ne excited species	Ne^* (sum of 3 s state), Ne_2^*
Xe excited species	Xe^* (sum of 6 s state), Xe^{**} (sum of 6 s' state), Xe_2^*
Dimer species	ArF^*, Ar_2F^*, $NeXe^*$, $XeAr^*$
Positive charged species	Ar^+, F_2^+, Ne^+, Xe^+, Ar_2^+, Ne_2^+, Xe_2^+, $NeXe^+$, $XeAr^+$
Negative charged species	F^-, e^-

Table 5. List of complete plasma reactions.

No.	Equations	Rate Coefficient ($1\,s^{-1}$, $m^3\,s^{-1}$, $m^6\,s^{-1}$)	Reference
	1) Electron impact reactions		
1	$Ar + e \rightarrow Ar + e$	$f(\sigma)$	[46]
2	$Ne + e \rightarrow Ne + e$	$f(\sigma)$	[46]
3	$F_2 + e \rightarrow F_2 + e$	$f(\sigma)$	[46]
4	$Xe + e \rightarrow Xe + e$	$f(\sigma)$	[46]
5	$F_2 + e \rightarrow F^- + F$	$f(\sigma)$	[46]
6	$Ar + e \rightarrow Ar^* + e$	$f(\sigma)$	[46]
7	$Ar + e \rightarrow Ar^{**} + e$	$f(\sigma)$	[46]
8	$Ne + e \rightarrow Ne^* + e$	$f(\sigma)$	[46]
9	$Xe + e \rightarrow Xe^* + e$	$f(\sigma)$	[46]
10	$Xe + e \rightarrow Xe^{**} + e$	$f(\sigma)$	[46]
11	$F_2 + e \rightarrow F_2^+ + e + e$	$f(\sigma)$	[46]
12	$Ar + e \rightarrow Ar^+ + e + e$	$f(\sigma)$	[46]
13	$Ne + e \rightarrow Ne^+ + e + e$	$f(\sigma)$	[46]
14	$Xe + e \rightarrow Xe^+ + e + e$	$f(\sigma)$	[46]
	2) Stepwise ionization		
15	$Ar^* + e \rightarrow Ar^+ + e + e$	$f(\sigma)$	[46]
16	$Ne^* + e \rightarrow Ne^+ + e + e$	$f(\sigma)$	[46]
17	$Xe^* + e \rightarrow Xe^+ + e + e$	$f(\sigma)$	[46]
18	$Ar^{**} + e \rightarrow Ar^+ + e + e$	$1.56 \times 10^{-13}\,(T_e[eV])^{0.71} \exp(-2.63/T_e[eV])$	[20]
19	$Xe^{**} + e \rightarrow Xe^+ + e + e$	$1.8 \times 10^{-13}\,(T_e[eV])^{0.61} \exp(-2.61/T_e[eV])$	[55]
20	$Ar_2^* + e \rightarrow Ar_2^+ + e + e$	$9.0 \times 10^{-14}\,(T_e[eV])^{0.70} \exp(-3.66/T_e[eV])$	[20]
21	$Ne_2^* + e \rightarrow Ne_2^+ + e + e$	$9.75 \times 10^{-15}\,(T_e[eV])^{0.71} \exp(-3.4/T_e[eV])$	[55]
22	$Xe_2^* + e \rightarrow Xe_2^+ + e + e$	$9.75 \times 10^{-14}\,(T_e[eV])^{0.71} \exp(-3.4/T_e[eV])$	[55]
23	$NeXe^* + e \rightarrow NeXe^+ + e + e$	$8.8 \times 10^{-14}\,(T_e[eV])^{0.71} \exp(-3.6/T_e[eV])$	[55]
	3) Combination ionization/Penning ionization		
24	$Ar^* + Ar^* \rightarrow Ar^+ + Ar + e$	5.0×10^{-16}	[20]
25	$Ar^* + Ar^{**} \rightarrow Ar^+ + Ar + e$	5.0×10^{-16}	[65]
26	$Ar^{**} + Ar^{**} \rightarrow Ar^+ + Ar + e$	5.0×10^{-16}	[20]
27	$Ar_2^* + Ar_2^* \rightarrow Ar2^+ + Ar + Ar + e$	5.0×10^{-16}	[20]
28	$Ne^* + Ne^* \rightarrow Ne^+ + Ne + e$	5.0×10^{-16}	[66]
29	$Ne_2^* + Ne_2^* \rightarrow Ne_2^+ + Ne + Ne + e$	5.0×10^{-16}	[66]
30	$Xe^* + Xe^* \rightarrow Xe^+ + Xe + e$	5.0×10^{-16}	[55]
31	$Xe^{**} + Xe^{**} \rightarrow Xe^+ + Xe + e$	5.0×10^{-16}	[55]
32	$Xe_2^* + Xe_2^* \rightarrow Xe_2^+ + Xe + Xe + e$	5.0×10^{-16}	[66]
33	$Ne^* + Ar \rightarrow Ar^+ + Ne + e$	6.5×10^{-17}	[47]
34	$Ne^* + Xe \rightarrow Xe^+ + Ne + e$	2.3×10^{-17}	[66]
35	$Ne^* + Xe \rightarrow NeXe^+ + e$	2.3×10^{-17}	[66]
36	$Ne_2^* + Ar \rightarrow Ar^+ + Ne + Ne + e$	6.5×10^{-17}	[47]
37	$Ne_2^* + Xe \rightarrow Xe^+ + Ne + Ne + e$	7.5×10^{-17}	[66]
38	$Ne_2^* + Xe \rightarrow NeXe^+ + Ne + e$	2.3×10^{-17}	[66]
39	$Ar^{**} + Xe \rightarrow Xe^+ + Ar + e$	2.0×10^{-16}	[66]

(Continued.)

Table 5. (Continued.)

No.	Equations	Rate Coefficient ($1\ s^{-1}$, $m^3\ s^{-1}$, $m^6\ s^{-1}$)	Reference
	4) Electron-ion recombination		
40	$Ar^+ + e \rightarrow Ar^{**}$	$4.0 \times 10^{-19}\,(T_e[eV])^{-0.5}$	[48]
41	$Ar^+ + e + e \rightarrow Ar^* + e$	$8.75 \times 10^{-39}\,(T_e[eV])^{-4.5}$	[49]
42	$Ar^+ + e + e \rightarrow Ar^{**} + e$	$5.0 \times 10^{-39}\,(T_e[eV])^{-4.5}$	[48]
43	$Ar^+ + e + Ar \rightarrow Ar^* + Ar$	1.0×10^{-38}	[50]
44	$Ar_2^+ + e \rightarrow Ar^* + Ar$	7.0×10^{-13}	[50]
45	$Ar_2^+ + e \rightarrow Ar^{**} + Ar$	$5.38 \times 10^{-14}\,(T_e[eV])^{-0.66}$	[48]
46	$Ne_2^+ + e \rightarrow Ne^* + Ne$	$3.7 \times 10^{-14}\,(T_e[eV])^{-0.43}$	[55]
47	$Xe^+ + e \rightarrow Xe$	6.4×10^{-13}	[50]
48	$Xe^+ + e + e \rightarrow Xe^{**} + e$	$5.1 \times 10^{-39}\,(T_e[eV])^{-4.5}$	[50]
49	$Xe_2^+ + e \rightarrow Xe^* + e$	3.7×10^{-14}	[48]
50	$Xe_2^+ + e \rightarrow Xe^{**} + e$	$3.33 \times 10^{-13}\,(T_e[eV])^{-0.5}$	[48]
51	$NeXe^+ + e \rightarrow Xe^* + Ne$	$2.0 \times 10^{-13}\,(T_e[eV])^{-0.5}$	[50]
52	$NeXe^+ + e \rightarrow Xe^{**} + Ne$	$8.0 \times 10^{-14}\,(T_e[eV])^{-0.5}$	[50]
53	$ArXe^+ + e \rightarrow Xe^* + Ar$	1.0×10^{-13}	[50]
	5) Electron impact de-excitation		
54	$Ar_2^* + e \rightarrow Ar + Ar + e$	1.0×10^{-13}	[20]
55	$ArF^* + e \rightarrow Ar + F + e$	2.0×10^{-13}	[51]
56	$Ar_2F^* + e \rightarrow Ar + Ar + F + e$	1.0×10^{-13}	[20]
57	$Ne_2^* + e \rightarrow Ne + Ne + e$	3.0×10^{-13}	[67]
58	$Xe_2^* + e \rightarrow Xe + Xe + e$	3.0×10^{-13}	[67]
59	$NeXe^* + e \rightarrow Ne + Xe + e$	3.0×10^{-13}	[67]
60	$ArXe^* + e \rightarrow Ar + Xe + e$	1.0×10^{-16}	[48]
	6) Ion-Ion recombination		
61	$Ar^+ + F^- \rightarrow ArF^*$	1.0×10^{-12}	[52]
62	$Ar_2^+ + F^- \rightarrow ArF^* + Ar$	1.0×10^{-12}	[52]
63	$F_2^+ + F^- \rightarrow F + F + F$	4.0×10^{-14}	[20]
64	$Ar^+ + F^- + M \rightarrow ArF^* + M$	$5.22 \times 10^{-11} \times N$	[47]
65	$Ar_2^+ + F^- + M \rightarrow ArF^* + Ar + M$	$5.45 \times 10^{-11} \times N$	[47]
66	$Ne^+ + F^- + M \rightarrow Ne + F + M$	$4.19 \times 10^{-11} \times N$	[47]
67	$Ne_2^+ + F^- + M \rightarrow Ne + Ne + F + M$	$4.82 \times 10^{-11} \times N$	[47]
	7) Charge transfer		
68	$Ar^+ + Xe \rightarrow Xe^+ + Ar$	4.3×10^{-19}	[48]
60	$Ar^+ + Ar + Ar \rightarrow Ar_2^+ + Ar$	2.5×10^{-43}	[48]
70	$Ar^+ + Ar + Xe \rightarrow Ar_2^+ + Xe$	2.0×10^{-43}	[48]
71	$Ar^+ + Ar + Ne \rightarrow Ne^+ + Ar + Ar$	1.6×10^{-44}	[53]
72	$Ar^+ + Xe + Xe \rightarrow ArXe^+ + Xe$	1.0×10^{-43}	[48]
73	$Ar^+ + Ar + Xe \rightarrow ArXe^+ + Ar$	1.0×10^{-43}	[48]
74	$Ar_2^+ + Xe \rightarrow Xe^+ + Ar + Ar$	1.25×10^{-43}	[48]
75	$Ne^+ + Ar \rightarrow Ar^+ + Ne$	1.0×10^{-17}	[54]
76	$Ne^+ + Xe \rightarrow Xe^+ + Ne$	1.0×10^{-17}	[55]
77	$Ne^+ + Ne + Ar \rightarrow Ne_2^+ + Ar$	1.0×10^{-43}	[55]
78	$Ne^+ + Ne + Ne \rightarrow Ne_2^+ + Ne$	4.4×10^{-44}	[55]
79	$Ne^+ + Ne + Xe \rightarrow Ne_2^+ + Xe$	8.0×10^{-44}	[54]
80	$Ne_2^+ + Ar \rightarrow Ar^+ + Ne + Ne$	5.0×10^{-20}	[55]
81	$Ne_2^+ + Xe \rightarrow Xe^+ + Ne + Ne$	1.0×10^{-16}	[54]
82	$Ne^+ + Ne + Xe \rightarrow NeXe^+ + Ne$	1.0×10^{-43}	[28]
83	$Ne_2^+ + Xe \rightarrow NeXe^+ + Ne$	1.0×10^{-19}	[28]
84	$Ne_2^+ + Ne + Xe \rightarrow Xe^+ + Ne + Ne + Ne$	4.0×10^{-42}	[28]
85	$Ne_2^+ + Ne + Ar \rightarrow Ar^+ + Ne + Ne + Ne$	1.0×10^{-43}	[54]
86	$Ne_2^+ + Ar + Ar \rightarrow Ar^+ + Ne + Ne + Ar$	1.0×10^{-43}	[54]
87	$Xe^+ + Xe + Ar \rightarrow Xe_2^+ + Ar$	2.0×10^{-43}	[55]
88	$Xe^+ + Xe + Ne \rightarrow Xe_2^+ + Ne$	2.5×10^{-43}	[55]
89	$Xe^+ + Xe + Xe \rightarrow Xe_2^+ + Xe$	2.5×10^{-43}	[48]

(Continued.)

Table 5. (Continued.)

No.	Equations	Rate Coefficient ($1\,s^{-1}$, $m^3\,s^{-1}$, $m^6\,s^{-1}$)	Reference
90	$Xe^+ + Ar + Ar \rightarrow ArXe^+ + Ar$	1.0×10^{-43}	[48]
91	$Xe^+ + Ne + Ne \rightarrow NeXe^+ + Ne$	2.5×10^{-43}	[68]
92	$NeXe^+ + Xe \rightarrow Xe2^+ + Ne$	5.0×10^{-18}	[67]
93	$NeXe^+ + Xe \rightarrow Xe^+ + Xe + Ne$	5.0×10^{-16}	[67]
94	$ArXe^+ + Ar \rightarrow Xe^+ + Ar + Ar$	$2.8 \times 10^{-13} \times \frac{300.0}{T_{gas}} \times \exp\left(\frac{-3007.0}{T_{gas}}\right)$	[69]
95	$ArXe^+ + Xe \rightarrow Xe^+ + Xe + Ar$	5.0×10^{-16}	[48]
96	$ArXe^+ + Xe \rightarrow Xe2^+ + Ar$	1.0×10^{-17}	[48]
	8) Two-body heavy particle reactions		
97	$Ar^* + F_2 \rightarrow ArF^* + F$	7.5×10^{-16}	[20]
98	$Ar^* + F_2 \rightarrow Ar + F + F$	3.1×10^{-16}	[20]
99	$Ar^* + Xe \rightarrow Xe^* + Ar$	2.2×10^{-16}	[50]
100	$Ar^* + Xe \rightarrow ArXe^*$	0.5×10^{-16}	[48]
101	$Ar^{**} + Ar \rightarrow Ar^* + Ar$	1.0×10^{-16}	[20]
102	$Ar^{**} + F_2 \rightarrow ArF^* + F$	4.7×10^{-16}	[20]
103	$Ar^{**} + F_2 \rightarrow Ar + F + F$	3.1×10^{-16}	[20]
104	$Ar^{**} + Xe \rightarrow Xe^* + Ar$	2.2×10^{-16}	[50]
105	$Ar^{**} + Xe \rightarrow ArXe^*$	0.5×10^{-16}	[48]
106	$Ar_2^* + F_2 \rightarrow Ar_2F^* + F$	2.5×10^{-16}	[20]
107	$Ar_2^* + F_2 \rightarrow ArF^* + F + Ar$	3.0×10^{-16}	[20]
108	$Ar_2^* + F \rightarrow ArF^* + Ar$	3.0×10^{-16}	[20]
109	$Ar_2^* + Xe \rightarrow Xe^* + Ar + Ar$	4.4×10^{-16}	[50]
110	$Ar_2^* + Xe \rightarrow ArXe^* + Ar$	0.5×10^{-16}	[48]
111	$Xe^* + Xe \rightarrow Xe + Xe$	3.5×10^{-15}	[50]
112	$Xe^* + Xe \rightarrow Xe^{**} + Xe$	1.5×10^{-15}	[50]
113	$Xe^{**} + Ar \rightarrow Xe^* + Ar$	1.0×10^{-10}	[50]
114	$Xe^{**} + Xe \rightarrow Xe^* + Xe$	2.8×10^{-13}	[50]
115	$ArF^* + Ar \rightarrow Ar + Ar + F$	9.0×10^{-18}	[20]
116	$ArF^* + F_2 \rightarrow Ar + F + F + F$	1.9×10^{-15}	[20]
117	$ArF^* + Ne \rightarrow Ar + F + Ne$	1.6×10^{-18}	[51]
118	$Ar_2F^* + Ar \rightarrow Ar + Ar + Ar + F$	2.2×10^{-20}	[65]
119	$Ar_2F^* + Ar \rightarrow ArF^* + Ar + Ar$	2.2×10^{-20}	[65]
120	$Ar_2F^* + F_2 \rightarrow Ar + Ar + F + F_2$	2.05×10^{-16}	[65]
121	$ArXe^* + Xe \rightarrow Xe_2^* + Ar$	1.0×10^{-16}	[48]
122	$NeXe^* + Xe \rightarrow Xe_2^* + Ne$	1.0×10^{-16}	[66]
	9) Three-body heavy particle reactions		
123	$Ar^* + Ar + Ar \rightarrow Ar_2^* + Ar$	1.14×10^{-44}	[20]
124	$Ar^* + Ar + Ne \rightarrow Ar_2^* + Ne$	1.1×10^{-44}	[47]
125	$Ar^* + Ar + Xe \rightarrow Ar_2^* + Xe$	1.10×10^{-44}	[48]
126	$Ar^* + Xe + Xe \rightarrow Xe_2^* + Ar$	1.10×10^{-45}	[48]
127	$Ar^{**} + Ar + Ar \rightarrow Ar_2^* + Ar$	1.14×10^{-44}	[48]
128	$Ar^{**} + Ar + Ne \rightarrow Ar_2^* + Ar$	1.0×10^{-44}	guess
129	$Ar^{**} + Ar + Xe \rightarrow Ar_2^* + Xe$	1.10×10^{-44}	[48]
130	$Ar^{**} + Xe + Xe \rightarrow Xe_2^* + Ar$	1.10×10^{-45}	[48]
131	$Ne^* + Ne + Ar \rightarrow Ne_2^* + Ar$	4.0×10^{-46}	guess
132	$Ne^* + Ne + Ne \rightarrow Ne_2^* + Ne$	8.0×10^{-46}	[55]
133	$Ne^* + Ne + Xe \rightarrow Ne_2^* + Xe$	4.0×10^{-46}	[55]
134	$Ne^* + Xe + Xe \rightarrow Xe_2^* + Ne$	1.0×10^{-45}	[55]
135	$Xe^* + Ar + Ar \rightarrow ArXe^* + Ar$	1.0×10^{-45}	[48]
136	$Xe^* + Xe + Ar \rightarrow Xe_2^* + Ar$	2.3×10^{-44}	[48]
137	$Xe^* + Xe + Ne \rightarrow Xe_2^* + Ne$	1.6×10^{-44}	[55]
138	$Xe^* + Xe + Xe \rightarrow Xe_2^* + Xe$	5.0×10^{-44}	[55]
139	$Xe^{**} + Xe + Ar \rightarrow Xe_2^* + Ar$	2.3×10^{-44}	[48]
140	$Xe^{**} + Xe + Ne \rightarrow Xe_2^* + Ne$	1.6×10^{-44}	[55]
141	$Xe^{**} + Xe + Xe \rightarrow Xe_2^* + Xe$	5.0×10^{-44}	[55]
142	$ArF^* + Ar + Ar \rightarrow Ar_2F^* + Ar$	4.0×10^{-43}	[51]

(Continued.)

Table 5. (Continued.)

No.	Equations	Rate Coefficient ($1\ s^{-1}$, $m^3\ s^{-1}$, $m^6\ s^{-1}$)	Reference
143	$ArF^* + Ar + Ar \rightarrow Ar + Ar + Ar + F$	5.0×10^{-44}	[65]
144	$ArF^* + Ar + Ne \rightarrow Ar_2F^* + Ne$	3.5×10^{-43}	[20]
145	$ArF^* + Ne + Ne \rightarrow Ar + F + Ne + Ne$	1.0×10^{-44}	[20]
	10) Radiation reactions		
146	$Ar_2^* \rightarrow Ar + Ar$	6.0×10^{7}	[20]
147	$ArF^* \rightarrow Ar + F$	2.5×10^{8}	[20]
148	$Ar_2F^* \rightarrow Ar + Ar + F$	5.4×10^{6}	[20]
159	$Ne_2^* \rightarrow Ne + Ne$	7.5×10^{7}	[55]
150	$Xe_2^* \rightarrow Xe + Xe$	7.2×10^{7}	[55]
151	$NeXe^* \rightarrow Ne + Xe$	5.0×10^{7}	[66]
152	$ArXe^* \rightarrow Ar + Xe$	5.0×10^{7}	[66]

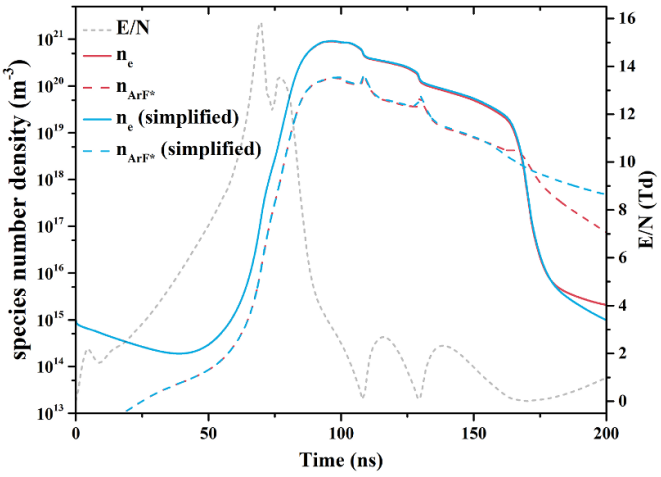

Figure 17. The comparison of n_e and n_{ArF^*} between the complete plasma chemistry (red lines) and the simplified plasma chemistry (blue lines).

ORCID iDs

Xiaochi Ma https://orcid.org/0000-0003-0951-9338
Yifei Zhu https://orcid.org/0000-0001-8989-0051
Yun Wu https://orcid.org/0000-0002-8575-0665

References

[1] Ito T and Okazaki S 2000 Pushing the limits of lithography *Nature* **406** 1027–31
[2] Kakizaki K, Sasaki Y, Inoue T and Sakai Y 2006 High-repetition-rate (6khz) and long-pulse-duration (50ns) arf excimer laser for sub-65nm lithography *Rev. Sci. Instrum.* **77** 035109
[3] Tsushima H Katsuumi H Ikeda H, Asayama T Kumazaki T, Kurosu A, Ohta T, Kakizaki K, Matsunaga T and Mizoguchi H 2014 Extremely long life and low-cost 193nm excimer laser chamber technology for 450mm wafer multipatterning lithography *Optical Microlithography XXVII* vol 9052 (SPIE) pp 411–8
[4] Kawasuji Y, Fujimoto J, Kobayashi M, Suwa A Mizutani A, Arakawa M, Onose T and Mizoguchi H 2020 Deep ultraviolet excimer laser processing for the micro via hole on semiconductor package *J. Laser Appl.* **32** 022076
[5] Okoshi M 2019 Fabrication of superhydrophobic silicone rubber with periodic micro/nano-suction cup structure by arf excimer laser-induced photodissociation *Nanomaterials* **9** 870
[6] Sugioka K, Akane T, Obata K Toyoda K and Midorikawa K 2002 Multiwavelength excitation processing using f2 and krf excimer lasers for precision microfabrication of hard materials *Appl. Surf. Sci.* **197** 814–21
[7] McAlinden C 2012 Corneal refractive surgery: past to present *Clin. Exp. Optometry* **95** 386–98
[8] Wolford M Myers M, Petrova T B, Giuliani J, Kessler T, McGeoch M, Petrov G, Schmitt A, Mehlhorn T and Obenschain S 2020 Development of a broad bandwidth 193 nanometer laser driver for inertial confinement fusion *High Energy Density Phys.* **36** 100801
[9] Obenschain S, Schmitt A, Bates J, Wolford M Myers M McGeoch M Karasik M and Weaver J 2020 Direct drive with the argon fluoride laser as a path to high fusion gain with sub-megajoule laser energy *Phil. Trans. R. Soc.* A **378** 20200031
[10] Panchenko A N, Sorokin D A and Tarasenko V F 2021 Gas lasers pumped by runaway electrons preionized diffuse discharge *Prog. Quantum Electron.* **76** 100314
[11] Dreiskemper R and Botticher W 1995 Current filamentation of strongly preionized high pressure glow discharges in ne/xe/hcl mixtures *IEEE Trans. Plasma Sci.* **23** 987–95
[12] Mathew D, Bastiaens H M, Boller K J and Peters P 2007 Effect of preionization, fluorine concentration and current density on the discharge uniformity in f2 excimer laser gas mixtures *J. Appl. Phys.* **102** 033305
[13] Feenstra L, Hoekstra O, Peters P and Witteman W 2000 On the performance of an arf and a krf laser as a function of the preionisation timing and the excitation mode *Appl. Phys.* B **70** 231–5
[14] Takahashi E, Kato S, Matsumoto Y and Okuda I 2010 Discharge instability induced by external laser preionization of a xef discharge laser *Appl. Phys.* B **98** 501–5
[15] Takahashi E, Kato S, Sasaki A, Kishimoto Y and Furutani H 2011 Controlling branching in streamer discharge by laser background ionization *J. Phys. D: Appl. Phys.* **44** 075204
[16] Maulhardt G, Schmidt K, Bartuch U and Vioel W 2007 Preionization of xef excimer laser by 248 nm laser beam *Laser Phys. Lett.* **4** 33–37
[17] Skrobol C, Heindl T, Krücken R, Morozov A, Steinhübl R, Wieser J and Ulrich A 2009 A miniature electron beam pumped laser *Eur. Phys. J.* D **54** 103–9
[18] Sethian J *et al* 1997 Large area electron beam pumped krypton fluoride laser amplifier *Rev. Sci. Instrum.* **68** 2357–66

[19] Kimura W, Guyer D R, Moody S, Seamans J and Ford D 1986 Electron density measurements of electron beam pumped xecl laser mixtures *Appl. Phys. Lett.* **49** 1569–71

[20] Kannari F, Obara M and Fujioka T 1985 An advanced kinetic model of electron-beam-excited krf lasers including the vibrational relaxation in krf*(b) and collisional mixing of krf*(b, c) *J. Appl. Phys.* **57** 4309–22

[21] Delmdahl R and Pätzel R 2013 Excimer laser technology trends *J. Phys. D: Appl. Phys.* **47** 034004

[22] Stephens J, Fierro A, Dickens J and Neuber A 2014 Influence of vuv illumination on breakdown mechanics: pre-ionization, direct photoionization and discharge initiation *J. Phys. D: Appl. Phys.* **47** 325501

[23] Feenstra L, Bastiaens H M, Peters P and Witteman W 1999 On the long pulse operation of an x-ray preionized, gas discharge pumped arf excimer laser *Appl. Phys. Lett.* **75** 1033–5

[24] Levko D, Yatom S, Vekselman V and Krasik Y E 2012 Electron emission mechanism during the nanosecond high-voltage pulsed discharge in pressurized air *Appl. Phys. Lett.* **100** 084105

[25] Levko D, Gurovich V T and Krasik Y E 2012 Numerical simulation of the pre-ionization processes during nanosecond-pulse discharge in nitrogen *J. Appl. Phys.* **111** 013306

[26] Azarov A, Peters P and Boller K-J 2008 Photoelectric effects in x-ray preionization for excimer laser gases *J. Appl. Phys.* **103** 043301

[27] Nijdam S, Takahashi E, Teunissen J and Ebert U 2014 Streamer discharges can move perpendicularly to the electric field *New J. Phys.* **16** 103038

[28] Ohwa M and Obara M 1986 Theoretical analysis of efficiency scaling laws for a self-sustained discharge pumped xecl laser *J. Appl. Phys.* **59** 32–41

[29] Demyanov A, Feenstra L, Peters P, Napartovich A and Witteman W 2001 Kinetic modelling of a discharge-pumped arf excimer laser and the effects of discharge filamentation *Appl. Phys.* B **72** 823–33

[30] Harrache Z and Belasri A 2007 Theoretical study of the pre-ionized xecl laser *J. Plasma Phys.* **73** 613–8

[31] Amir Aid D, Harrache Z and Belasri A 2007 Study of streamer development in high-pressure electric discharge: Applications to excimer lasers *Laser Phys.* **17** 12–17

[32] Yampolskaya S A, Yastremskii A G, Panchenko Y N, Puchikin A V and Bobrovnikov S M 2020 Numerical study of the discharge spatial characteristics influence on the krf laser generation *IEEE J. Quantum Electron.* **56** 1–9

[33] Chen J, Zhao Z Liu Z and Fu Y 2024 Effects of tunable circuit parameters on pulsed discharge and input-output characteristics of a xecl excimer laser *J. Phys. D: Appl. Phys.* **57** 135202

[34] Xiong Z and Kushner M J 2010 Surface corona-bar discharges for production of pre-ionizing uv light for pulsed high-pressure plasmas *J. Phys. D: Appl. Phys.* **43** 505204

[35] Xiong Z and Kushner M J 2011 Photo-triggering and secondary electron produced ionization in electric discharge arf* excimer lasers *J. Appl. Phys.* **110** 083304

[36] Li C, Brok W, Ebert U and Van der Mullen J 2007 Deviations from the local field approximation in negative streamer heads *J. Appl. Phys.* **101** 123305

[37] Grubert G, Becker M and Loffhagen D 2009 Why the local-mean-energy approximation should be used in hydrodynamic plasma descriptions instead of the local-field approximation *Phys. Rev.* E **80** 036405

[38] Zhu Y, Shcherbanev S, Baron B and Starikovskaia S 2017 Nanosecond surface dielectric barrier discharge in atmospheric pressure air: I. measurements and 2d modeling of morphology, propagation and hydrodynamic perturbations *Plasma Sources Sci. Technol.* **26** 125004

[39] Zhu Y, Chen X, Wu Y, Hao J, Ma X, Lu P and Tardiveau P 2021 Simulation of ionization-wave discharges: a direct comparison between the fluid model and e-fish measurements *Plasma Sources Sci. Technol.* **30** 075025

[40] Hagelaar G and Pitchford L C 2005 Solving the boltzmann equation to obtain electron transport coefficients and rate coefficients for fluid models *Plasma Sources Sci. Technol.* **14** 722

[41] Almeida P, Benilov M and Naidis G 2002 Calculation of ion mobilities by means of the two-temperature displaced-distribution theory *J. Phys. D: Appl. Phys.* **35** 1577

[42] Peskin C S 2002 The immersed boundary method *Acta Numer.* **11** 479–517

[43] Celestin S, Bonaventura Z, Zeghondy B, Bourdon A and Ségur P 2009 The use of the ghost fluid method for poisson's equation to simulate streamer propagation in point-to-plane and point-to-point geometries *J. Phys. D: Appl. Phys.* **42** 065203

[44] Zhu Y and Starikovskaia S 2018 Fast gas heating of nanosecond pulsed surface dielectric barrier discharge: Spatial distribution and fractional contribution from kinetics *Plasma Sources Sci. Technol.* **27** 124007

[45] Pancheshnyi S 2007 Experimental study, direct nimerical simulation and application of ionization wave *PhD Thesis* University Paul Sabatier (Toulouse III)

[46] Pitchford L C *et al* 2017 Lxcat: An open-access, web-based platform for data needed for modeling low temperature plasmas *Plasma Process. Polymers* **14** 1600098

[47] Lee Y-W, Matsui E, Kannari F and Obara M 1989 Theoretical high-efficiency extraction study of a short-pulse electron-beam-pumped arf laser amplifier with atmospheric pressure ar-rich mixtures *IEEE J. Quantum Electron.* **25** 2053–66

[48] Bhoj A N and Kushner M J 2004 Avalanche process in an idealized lamp: Ii. modelling of breakdown in ar/xe electric discharges *J. Phys. D: Appl. Phys.* **37** 2510

[49] Kolev S and Bogaerts A 2014 A 2d model for a gliding arc discharge *Plasma Sources Sci. Technol.* **24** 015025

[50] Min B-K, Lee S-H and Park H-G 2000 New combination of a three-component gas, ne–xe–ar, for a high efficiency plasma display panel *J. Vac. Sci. Technol.* A **18** 349–55

[51] Bochenko A, Derzhiev V I, Zhidkov A and Yakovlenko S I 1992 Kinetic model of an arf laser *Sov. J. Quantum Electron.* **22** 444

[52] Greene A and Brau C 1978 Theoretical studies of uv-preionized transverse discharge krf and arf lasers *IEEE J. Quantum Electron.* **14** 951–7

[53] Boichenko A Karelin A and Yakovlenko S I 1995 Kinetic model of xef laser *Int. Conf. on Atomic and Molecular Pulsed Laser* vol 2619 (SPIE) pp 211–5

[54] Boichenko A M and Yakovlenko S I 2000 The possibility of lasing in ne+ ar ionic molecules pumped by a hard ioniser *Quantum Electron.* **30** 681

[55] Rauf S and Kushner M J 1999 Dynamics of a coplanar-electrode plasma display panel cell. i. basic operation *J. Appl. Phys.* **85** 3460–9

[56] Pancheshnyi S 2014 Photoionization produced by low-current discharges in o2, air, n2 and co2 *Plasma Sources Sci. Technol.* **24** 015023

[57] Takahashi E, Kato S, Okuda I and Matsumoto Y 2009 Influence of multi-photon ionization of xe on a xef discharge induced by krf laser irradiation *Appl. Phys.* B **97** 511–4

[58] Chan W, Cooper G, Guo X, Burton G and Brion C 1992 Absolute optical oscillator strengths for the electronic

excitation of atoms at high resolution. III. The photoabsorption of argon, krypton and xenon *Phys. Rev.* A **46** 149
[59] Chan W, Cooper G, Guo X and Brion C 1992 Absolute optical oscillator strengths for the electronic excitation of atoms at high resolution. ii. the photoabsorption of neon *Phys. Rev.* A **45** 1420
[60] Morozov A, Heindl T, Krücken R, Ulrich A and Wieser J 2008 Conversion efficiencies of electron beam energy to vacuum ultraviolet light for ne, ar, kr and xe excited with continuous electron beams *J. Appl. Phys.* **103** 103301
[61] Zhu Y Wu Y and Li J 2020 Photopic: calculate photo-ionization functions and model coefficients for gas discharge simulations (arXiv:2005.10021)
[62] Bourdon A, Pasko V, Liu N Y, Célestin S, Ségur P and Marode E 2007 Efficient models for photoionization produced by non-thermal gas discharges in air based on radiative transfer and the helmholtz equations *Plasma Sources Sci. Technol.* **16** 656
[63] Babaeva N Y, Naidis G, Tereshonok D and Son E 2018 Development of nanosecond discharges in atmospheric pressure air: two competing mechanisms of precursor electrons production *J. Phys. D: Appl. Phys.* **51** 434002
[64] Zhu Y, Lepikhin N D, Orel I S, Salmon A Klochko A V and Starikovskaia S M 2018 Optical actinometry of o-atoms in pulsed nanosecond capillary discharge: peculiarities of kinetics at high specific deposited energy *Plasma Sources Sci. Technol.* **27** 075020
[65] Petrova T B, Wolford M, Myers M and Obenschain S 2023 Modeling of the NRL electra electron-beam pumped argon fluoride laser *IEEE Trans. Plasma Sci.* **51** 1392–403
[66] Johnson T H, Cartland H E, Genoni T C and Hunter A M 1989 A comprehensive kinetic model of the electron-beam-excited xenon chloride laser *J. Appl. Phys.* **66** 5707–25
[67] Levin L, Moody S, Klosterman E, Center R and Ewing J 1981 Kinetic model for long-pulse xecl laser performance *IEEE J. Quantum Electron.* **17** 2282–9
[68] Hokazono H, Midorikawa K, Obara M and Fujioka T 1984 Theoretical analysis of a self-sustained discharge pumped xecl laser *J. Appl. Phys.* **56** 680–90
[69] Apruzese J Giuliani J, Wolford M, Sethian J, Petrov G, Hinshelwood D, Myers M, Ponce D, Hegeler F and Petrova T 2006 Experimental evidence for the role of xe2+ in pumping the ar–xe infrared laser *Appl. Phys. Lett.* **88** 121120